

1 **Bias correction and statistical modeling of variable**
2 **oceanic forcing of Greenland outlet glaciers**

3 **Vincent Verjans¹, Alexander Robel¹, Andrew F. Thompson², and Helene**
4 **Seroussi³**

5 ¹School of Earth and Atmospheric Sciences, Georgia Institute of Technology, Atlanta, GA, USA

6 ²Environmental Science and Engineering, California Institute of Technology, Pasadena, CA 91125, USA

7 ³Thayer School of Engineering, Dartmouth College, Hanover, NH, USA

8 **Key Points:**

- 9
- 10 • We develop a statistical method to generate ocean forcing boundary conditions
for Greenland ice sheet model simulations.
 - 11 • The method bias-corrects and extrapolates global climate model output using re-
12 analysis products and high-resolution model results.
 - 13 • Stochastic time series models reproduce the spatiotemporal variability of ocean
14 conditions at negligible computational expense.

Corresponding author: Vincent Verjans, vverjans3@gatech.edu

Abstract

Variability in oceanic conditions directly impacts ice loss from marine outlet glaciers in Greenland, influencing the ice sheet mass balance. Oceanic conditions are available from Atmosphere-Ocean Global Climate Model (AOGCM) output, but these models require extensive computational resources and lack the fine resolution needed to simulate ocean dynamics on the Greenland continental shelf and close to glacier marine termini. Here, we develop a statistical approach to generate ocean forcing for ice sheet model simulations, which incorporates natural spatiotemporal variability and anthropogenic changes. Starting from raw AOGCM ocean heat content, we apply: (1) a bias-correction using ocean reanalysis, (2) an extrapolation accounting for on-shelf ocean dynamics, and (3) stochastic time series models to generate realizations of natural variability. The bias-correction reduces model errors by $\sim 25\%$ when compared to independent in-situ measurements. The bias-corrected time series are subsequently extrapolated to fjord mouth locations using relations constrained from available high-resolution regional ocean model results. The stochastic time series models reproduce the spatial correlation, characteristic timescales, and the amplitude of natural variability of bias-corrected AOGCMs, but at negligible computational expense. We demonstrate the efficiency of this method by generating >6000 time series of ocean forcing for >200 Greenland marine-terminating glacier locations until 2100. As our method is computationally efficient and adaptable to any ocean model output and reanalysis product, it provides flexibility in exploring sensitivity to ocean conditions in Greenland ice sheet model simulations. We provide the output and workflow in an open-source repository, and discuss advantages and future developments for our method.

Plain Language Summary

Model simulations of the Greenland ice sheet require knowledge of ocean conditions. The evolution of ocean conditions has a strong impact on ice sheet model predictions, as there are more than 200 glaciers in Greenland flowing directly into the ocean. However, modeling oceanic forcing is difficult. The state-of-the-art approach is to use output from Atmosphere-Ocean Global Climate Models (AOGCMs). But these models cannot accurately capture the ocean dynamics on the Greenland shelf, and they can show strong biases compared to observations. Furthermore, AOGCMs are computationally expensive, meaning that it is impossible to thoroughly characterize the uncertainty associated with the chaotic nature of climate. Here, we propose a procedure to bias-correct and extrapolate oceanic output from AOGCMs. Our method exploits observational datasets, as well as available high-resolution ocean model results. Using statistical models, we reproduce patterns of spatiotemporal ocean variability at low computational expense, and represent internal climate variability and global warming trends. The goal is to provide a scalable procedure to generate ocean forcing for long-term Greenland ice sheet model predictions.

1 Introduction

Since 1992, Greenland ice sheet (GrIS) mass loss has contributed ~ 0.4 mm yr^{-1} to global mean sea-level rise (IMBIE, 2020). Mass losses are approximately equally partitioned between increased surface melt runoff and increased ice discharge into the ocean, although variability in the contribution of these two processes is strongly linked to temporal variability in climatic forcing (Mouginot et al., 2019). In particular, increased ice discharge has been linked to warming oceanic conditions (Holland et al., 2008; Walsh et al., 2012; Straneo & Heimbach, 2013; Porter et al., 2018; Wood et al., 2021). Increased ice loss at outlet glacier termini causes glacier thinning and speed-up, thus inducing longer-term dynamic responses in the ice sheet interior (Nick et al., 2009; Felikson et al., 2017). Changes in ocean temperatures, and their link to increased outlet glacier mass loss rates,

65 are therefore expected to exert a major control on future GrIS mass balance (Wood et
66 al., 2021).

67 Melting of marine-terminating glaciers is driven by relatively warm deep waters of
68 Atlantic origin (Straneo & Heimbach, 2013; Sutherland et al., 2013). However, heat deliv-
69 ery to outlet glacier termini depends on water circulation across the continental shelf
70 and within fjords. Waters of Atlantic origin are transported onto the shelf mostly via
71 cross-shelf troughs (Rignot et al., 2012; Sutherland et al., 2013). Oceanic heat found at
72 the shelf break can be restricted from reaching glacier termini due to several factors. First,
73 heat can be eroded due to vertical mixing. Second, the presence of sills can block the
74 access of Atlantic waters into fjords (Straneo et al., 2012; Straneo & Cenedese, 2015; Jack-
75 son et al., 2018). Finally, close to the glacier termini, several convective processes can
76 influence heat availability for glacier melt, such as subglacial discharge (Slater et al., 2018),
77 wind-driven flow (Jackson et al., 2014; Sutherland et al., 2014; Jackson et al., 2018), and
78 sea-ice formation (Cottier et al., 2010). All of these local processes over the continen-
79 tal shelf contribute to setting the characteristic variability of ocean thermal forcing.

80 While ice sheet model simulations of Greenland outlet glaciers are sensitive to oceanic
81 forcing, no Greenland-scale ocean model completely captures the range of processes and
82 time scales governing ocean heat transfer to glacier termini (Slater et al., 2020). Even
83 the highest-resolution regional ocean model simulations do not capture all the kilome-
84 ter to sub-kilometer scale processes at play, and they only extend over periods shorter
85 than 20 yr (e.g., Rignot et al., 2012; Gillard et al., 2016). In this context, Greenland ice
86 sheet model predictions use ocean forcing input provided by Atmosphere-Ocean Gen-
87 eral Circulation Models (AOGCMs), because they cover periods until 2100 and beyond.
88 However, due to their coarse resolution in the ocean (typically $1^\circ \times 1^\circ$), they cannot sim-
89 ulate fjord processes, and their representation of on-shelf ocean dynamics is incomplete
90 (Slater et al., 2020). Because of the current inability to fully resolve fjord dynamics within
91 large-scale ocean models, Xu et al. (2012) and Rignot et al. (2016) developed a param-
92 eterization of glacier melt based on an empirical relation found with water temperatures
93 at the fjord mouth and subglacial discharge. This parameterization has not been cali-
94 brated to measurements from outlet glaciers, but to idealized fjord-scale model simula-
95 tions. Another parameterization, adapted to coarse-resolution AOGCM output, has been
96 developed for use in ice sheet models by linking regionally-averaged ocean temperatures
97 to individual glacier terminus positions (Cowton et al., 2018; Slater et al., 2019). The
98 latest Ice Sheet Model Intercomparison for CMIP6 (ISMIP6) for Greenland has proposed
99 these two types of parameterizations: prescribing either terminus position or glacier frontal
100 melt as a function of far-field ocean temperature averaged over large regional oceanic sec-
101 tors (Goelzer et al., 2020; Slater et al., 2020). While computationally convenient, the ter-
102 minus position parameterization neglects feedback effects from ice flow dynamics and bed
103 topography on outlet glacier dynamics, and its empirical parameter is highly uncertain
104 (Slater et al., 2019, 2020). Furthermore, the parameterization relies on far-field ocean
105 temperature, thus neglecting variability associated with shelf processes in heat transport
106 towards the fjords. The direct ice melt rate parameterization, on the other hand, allows
107 ice sheet models to resolve interactions between melt and calving rates, but remains to
108 be validated against large-scale Greenland outlet glaciers observations. It also relies on
109 the assumption that AOGCMs can provide accurate ocean temperature fields at the en-
110 try of fjord mouths, which corresponds to areas where fine-scale dynamical and topo-
111 graphical details cannot be resolved in coarse resolution models.

112 Finally, current ice sheet model predictions neglect internal variability in ocean con-
113 ditions, as they generally use a single deterministic AOGCM output to represent future
114 oceanic conditions. ISMIP6 accounted for inter-AOGCM uncertainty and greenhouse gas
115 emission-scenario dependence by using six different AOGCMs, one of which included both
116 a high- and low-emission scenario (Goelzer et al., 2020; Slater et al., 2020). However, dif-
117 ferent runs from the same AOGCM starting with only round-off level errors in initial con-

118 conditions can exhibit large differences in patterns of climate variability over a range of timescales
 119 (Kay et al., 2015; Maher et al., 2019). This internal variability is caused by the chaotic
 120 nature of the climate system (Hasselmann, 1976). Due to the computational expense of
 121 AOGCM simulations, the number of different simulations from a given AOGCM is limited,
 122 making it challenging to directly force ice sheet models with a model ensemble of
 123 climatic forcings representative of internal climate variability. To date, the most comprehensive
 124 evaluation of internal ocean variability impact on GrIS simulations has been
 125 performed by Tsai et al. (2017), as they used the coarse-resolution ocean output of 50
 126 realizations from a same AOGCM. An alternative approach to quantify the impact of
 127 internal variability is to calibrate statistical models to a small set of AOGCM runs (e.g.,
 128 Castruccio & Stein, 2013; Hu & Castruccio, 2021), which can then be used to generate
 129 stochastic climatic forcing within ice sheet models (Verjans et al., 2022).

130 Using AOGCMs to provide long-term ocean forcing for ice sheet models thus faces
 131 the limitations of horizontal resolution and characterization of internal variability. Furthermore,
 132 bias-correction techniques are needed due to AOGCM disagreement with in-situ
 133 observational data (Slater et al., 2019), but currently-used techniques are simplistic
 134 compared to methods applied in other climate model applications (e.g., Cui et al.,
 135 2012). There is a stark contrast between the level of refinement of atmospheric forcing
 136 compared to ocean forcing used in Greenland ice sheet simulations. For atmospheric forcing,
 137 there exists a large number of high-resolution models to downscale AOGCM output,
 138 which are specifically calibrated to ice sheet processes (Fettweis et al., 2020). Dynamical
 139 downscaling allows to resolve small scale processes over Greenland, while being forced by
 140 AOGCM large scale fields at the domain boundaries. Some models even associate this dynamical
 141 downscaling with a statistical downscaling process (Noël et al., 2016). In contrast, no high-resolution
 142 ocean model or downscaling method have been used to generate ocean forcing for Greenland ice
 143 sheet model simulations in any prior studies, although such methods have been applied to ocean
 144 models for other applications (e.g., Camus et al., 2014; Oliver & Holbrook, 2014; Fagundes et al.,
 145 2020).

146 In this study, we outline a statistical method to compute ocean thermal forcing for
 147 outlet glaciers in Greenland ice sheet model simulations. We describe the methodological
 148 details, present results from application of the method, and discuss advantages and
 149 possible future developments. We provide the code and many different outputs in an open
 150 source repository (see *Open Research*).

151 2 Methods

The overarching objective of this study is to generate the most representative realizations of ocean thermal forcing (TF) at the fjord mouth of Greenland outlet glaciers. We describe a general method to achieve this, starting from the ocean temperature and salinity outputs of any AOGCM. The variable of interest is TF , which is defined as the ocean temperature above the freezing point. To calculate TF , we use the salinity- and depth-dependent empirical equation for the freezing point from Cowton et al. (2015):

$$TF(\mathbf{x}, t) = T_{oc}(\mathbf{x}, t) - (\lambda_1 S_{oc}(\mathbf{x}, t) + \lambda_2 + \lambda_3 z), \quad (1)$$

152 where T_{oc} is the ocean temperature [$^{\circ}\text{C}$], S_{oc} is the ocean salinity [psu], z is depth [m,
 153 positive upwards], and $\lambda_1, \lambda_2, \lambda_3$ are parameters set to $-5.73 \times 10^{-2} \text{ } ^{\circ}\text{C} \text{ psu}^{-1}$, $8.32 \times$
 154 $10^{-2} \text{ } ^{\circ}\text{C}$, and $-7.61 \times 10^{-4} \text{ } ^{\circ}\text{C} \text{ m}^{-1}$, respectively. The dependence on space and time
 155 is highlighted by \mathbf{x} and t , respectively.

156 We average TF between the surface and 500 m depth: TF_{0-500} . At gridpoints where
 157 the bathymetry is shallower than 500 m, TF_{0-500} only accounts for TF values ranging
 158 between 0 m and the seafloor depth. However, we discard gridpoints where the bathymetry
 159 is less than 100 m deep to generate our datasets of TF_{0-500} , as the coarse resolution AOGCMs

160 do not capture the fine details of bathymetry in these areas. As such, our computation
 161 of TF_{0-500} at any gridpoint i, j with bathymetry $B_{i,j}$ is defined as:

$$TF_{0-500} = \frac{1}{|\max(B_{i,j}, -500)|} \int_{\max(B_{i,j}, -500)}^0 TF(z) dz \quad \text{if } B_{i,j} \leq -100. \quad (2)$$

162 Our approach differs from the approach of Slater et al. (2019, 2020), as they av-
 163 eraged TF only between 200 and 500 m depth ($TF_{200-500}$). The 0-500 m depth range
 164 is chosen here to remain consistent with the derivation of the melt parameterization of
 165 Xu et al. (2012). Furthermore, on a large part of the Greenland continental shelf, the
 166 0-200 m depth range is an important fraction of the water column (Morlighem et al., 2017,
 167 see also Fig.1a). As such, TF_{0-200} is potentially an important contributor to variabil-
 168 ity in thermal forcing for Greenland outlet glaciers, although these waters are often colder
 169 and fresher than deeper Atlantic waters. However, the method outlined in this study can
 170 easily be reproduced choosing any depth range over which TF is averaged, which can
 171 serve different applications. In particular, it is possible to process TF separately over
 172 different depth ranges to study shallower Arctic waters and deeper Atlantic waters sep-
 173 arately. In the following, we drop the subscript 0-500 to simplify the notation, but any
 174 TF symbol stands for TF_{0-500} as defined in Eq. (2).

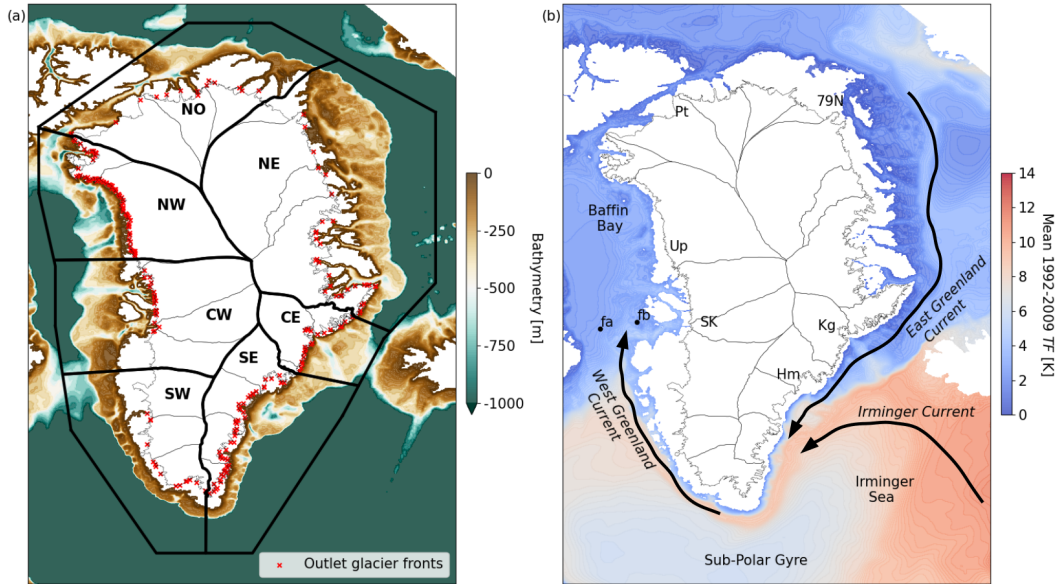


Figure 1. Maps of Greenland with (a) bathymetry and (b) mean (1992-2009) TF from ECCO (Nguyen et al., 2012). The ECCO bathymetry uses a merged product of the blend S2004 (Marks & Smith, 2006) and International Bathymetric Chart of the Arctic Ocean (Jakobsson et al., 2008). In (a), we show the delineation of the 7 oceanic sectors that constitute the ocean domain for this study and the 226 marine-terminating outlet glacier front locations. The sectors are taken from Slater et al. (2019), but the SE and SW sectors are extended 100 km southwards. The outlet glacier fronts are from Wood et al. (2021). In (b), we show major locations mentioned in this study. Glaciers are Kg: Kangerlussuaq, Hm: Helheim, SK: Sermeq Kujalleq, Up: Upernavik, Pt: Petermann, 79N: 79 North. The points fa and fb show locations of gridpoints used in Fig (5a) and (5b), respectively.

175 Our methodology to generate TF time series based on AOGCM TF output con-
 176 sists of three separate steps, which are outlined in Figure 2, and multiple data and model
 177 products, which are summarized in Table 1. The first step is to use an ocean reanaly-
 178 sis product, which is constrained by observations, to correct the AOGCM bias and to
 179 constrain its temporal variability in TF (first key step in Fig. 2). This statistical cor-
 180 rection is performed via Quantile Delta Mapping, which is a method detailed in Section
 181 2.1. The second step is to extrapolate the corrected AOGCM TF from the open ocean
 182 to inshore, i.e., at the mouths of fjords on the Greenland shelf (second key step in Fig.
 183 2). This extrapolation process uses constraints derived from output of a high-resolution
 184 regional ocean model and accounts for different offshore-inshore relationships at differ-
 185 ent timescales of variability, as explained in Section 2.2. The final step is to calibrate sta-
 186 tistical time series models to the variability of the corrected and extrapolated TF ob-
 187 tained after the first two steps (third key step in Fig. 2). This calibration procedure, de-
 188 tailed in Section 2.3, effectively reproduces the stochastic variability in ocean heat con-
 189 tent, while preserving deterministic signals such as means, trends, and seasonality pat-
 190 terns. Ultimately, our method constructs statistical models capable of generating large
 191 numbers of realizations of TF for Greenland glaciers. This study uses specific data and
 192 model products, described in Table 1, but allows great flexibility in the particular choice
 193 of these products.

Type of product	Used in this study	Used for	Sections	Temporal coverage	Horizontal resolution	Reference
AOGCM	MIROC-ES2L	Raw TF	2.1, 2.2, 2.3	1850-2100	1°	Hajima et al. (2020)
AOGCM	IPSL-CM6A	Raw TF	2.1, 2.2, 2.3	1850-2100	1°	Boucher et al. (2020)
Reanalysis	EN4 objective analyses	Quantile Delta Mapping (QDM)	2.1	1900-2022	1°	Good et al. (2013)
High-resolution ocean model	ECCO-Arctic	Offshore to inshore extrapolation	2.2	1992-2009	4 km	Nguyen et al. (2012)
In-situ data	CTD	Evaluation of QDM	3.1	2000-2015	/	Good et al. (2013)

Table 1. Model and data products required in our method, and the examples of specific products used for this study (TF : thermal forcing).

194 2.1 Statistical correction of thermal forcing

195 The first step in our method is to bias-correct the AOGCM TF to the mean, sea-
 196 sonality, and interannual variability of a reference dataset. To illustrate our method, the
 197 reference dataset used is the Hadley Centre EN4.2.1 monthly objective analyses (Good
 198 et al., 2013), hereafter referred to as EN4. EN4 is a gridded product at 1° resolution cover-
 199 ing 1900-2022. The EN4 method uses a local interpolation of Conductivity-Temperature-
 200 Depth (CTD) profile measurements combined to a background persistence from damped
 201 anomalies of the previous month; we refer to Good et al. (2013) for the methodological
 202 details. While it may be questionable to use a reanalysis product as the ground-truth
 203 dataset for a statistical correction, we note several advantages of the EN4 monthly ob-
 204 jective analyses. First, EN4 is an interpolated product of oceanographic profile data. In
 205 contrast to other reanalysis products that use a dynamical model with data assimilation,
 206 EN4 is more strongly constrained by observations, ensuring better agreement with in-
 207 situ data. On the other hand, it implies that EN4 interpolates between observations with-
 208 out dynamical constraints, and is more prone to errors in case of observational uncer-
 209 tainties and if some periods and/or regions have sparse observational coverage. Second,
 210 the long temporal coverage provides more robust statistics than from most other reanal-
 211 ysis products. The long response timescales of ocean dynamics imply that at least sev-
 212 eral decades are needed to capture oceanic mean conditions and variability. Still, we note

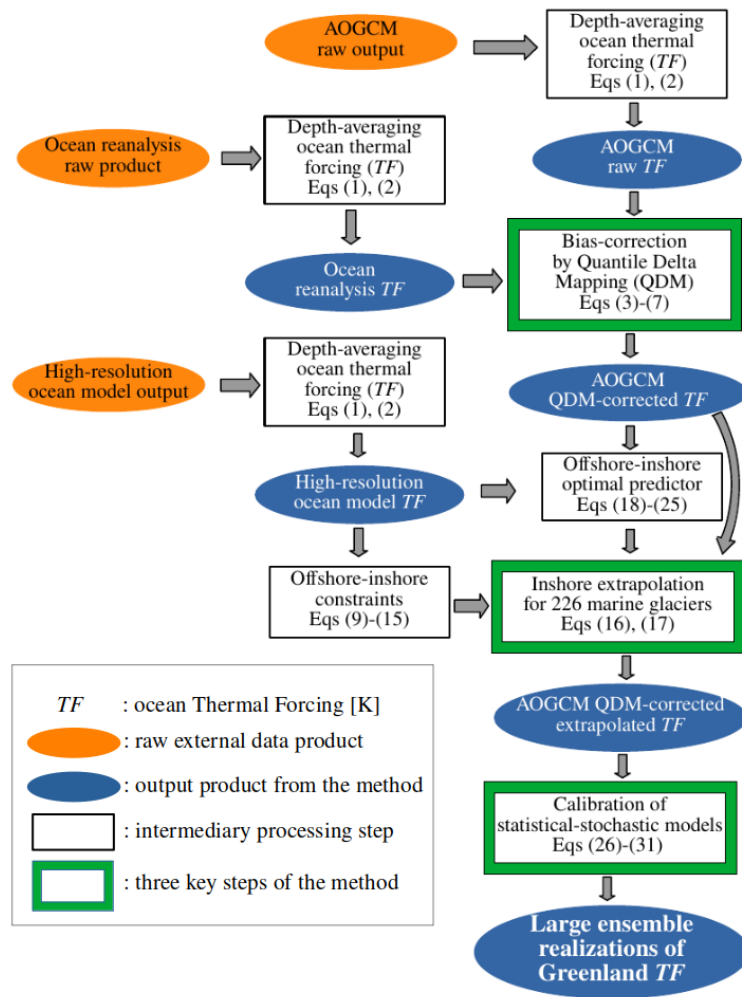


Figure 2. Flowchart of the methodology. The final output is a large ensemble of realizations of Greenland oceanic conditions at all the marine terminating glaciers.

213 that the bias-correction could equally well be performed with other gridded ocean re-
 214 analysis products in place of the EN4 objective analyses.

215 We use both the temperature and salinity products from EN4 to compute a monthly
 216 gridded TF field, following Eq. (1). We discard EN4 gridpoints if the TF time series has
 217 negative values. EN4 also provides an observational weight variable, which varies between
 218 0 and 1 depending on how strongly EN4 is constrained by observations (see Good et al.,
 219 2013). We average the observational weights over large areas: the 7 oceanic sectors around
 220 Greenland used by Slater et al. (2019): North (NO), North-East (NE), Central-East (CE),
 221 South-East (SE), South-West (SW), Central-West (CW), and North-West (NW) (see Fig.1a).
 222 We extend the SE and SW sectors 100 km southwards because the original sector de-
 223 lineations only cover two to three gridpoints of EN4 in the meridional direction. In Fig-
 224 ure 3, the sector-averaged observational weights clearly show a shift around 1950, with
 225 oceanic properties being significantly better constrained from this date. For this reason,
 226 we elect 1950 as the starting date for the calibration period, and we discard the 1900-
 227 1950 data. Nevertheless, EN4 observational weights are consistently lower in winter months,
 228 due to sparser in-situ data collection. We correct TF time series of individual AOGCM
 229 gridpoints over their period overlapping the 1950-2022 period. In the Coupled Model In-
 230 tercomparison Project 6 (CMIP6) framework, historical model experiments cover the pe-
 231 riod 1850-2015, and model results post-2015 depend on the emission scenario assumed.
 232 Thus, our period for calibrating AOGCM TF is 1950-2015. Any given AOGCM grid-
 233 point is corrected with the nearest neighbor EN4 TF time series. The statistical correc-
 234 tion requires time series of data, and can therefore not be performed with in-situ data
 235 only, which are sparse in time and space.

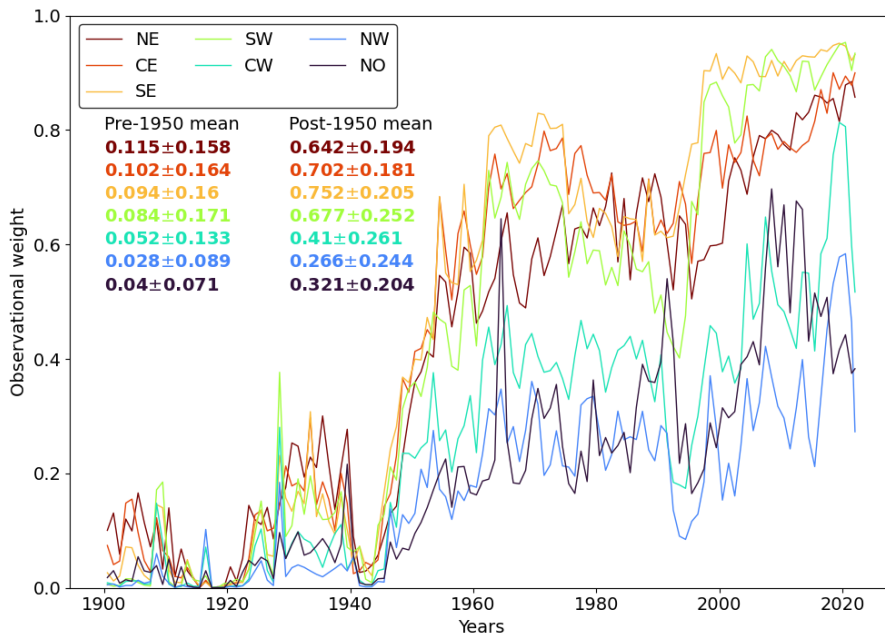


Figure 3. Observational weight variable of the EN4 objective analyses (Good et al., 2013) averaged yearly and by oceanic sector. Higher values of observational weight denote periods better constrained with in-situ measurements. Sector-averaged pre- and post-1950 mean values of the observational weight are displayed, with ± 1 standard deviation.

236 The motivation for correcting AOGCM outputs is that they may misrepresent the
 237 mean and/or variability in TF . Figure 4 shows biases between EN4 and two AOGCMs

238 that participated to ISMIP6. On the Greenland shelf, the biases in mean TF and TF
 239 standard deviation typically range between $[-4;4]$ K and $[-1.5;0.5]$ K, respectively (Fig.
 240 4). While the bias in the mean varies geographically and between the two AOGCMs, both
 241 of them generally underestimate TF variability when compared to EN4.

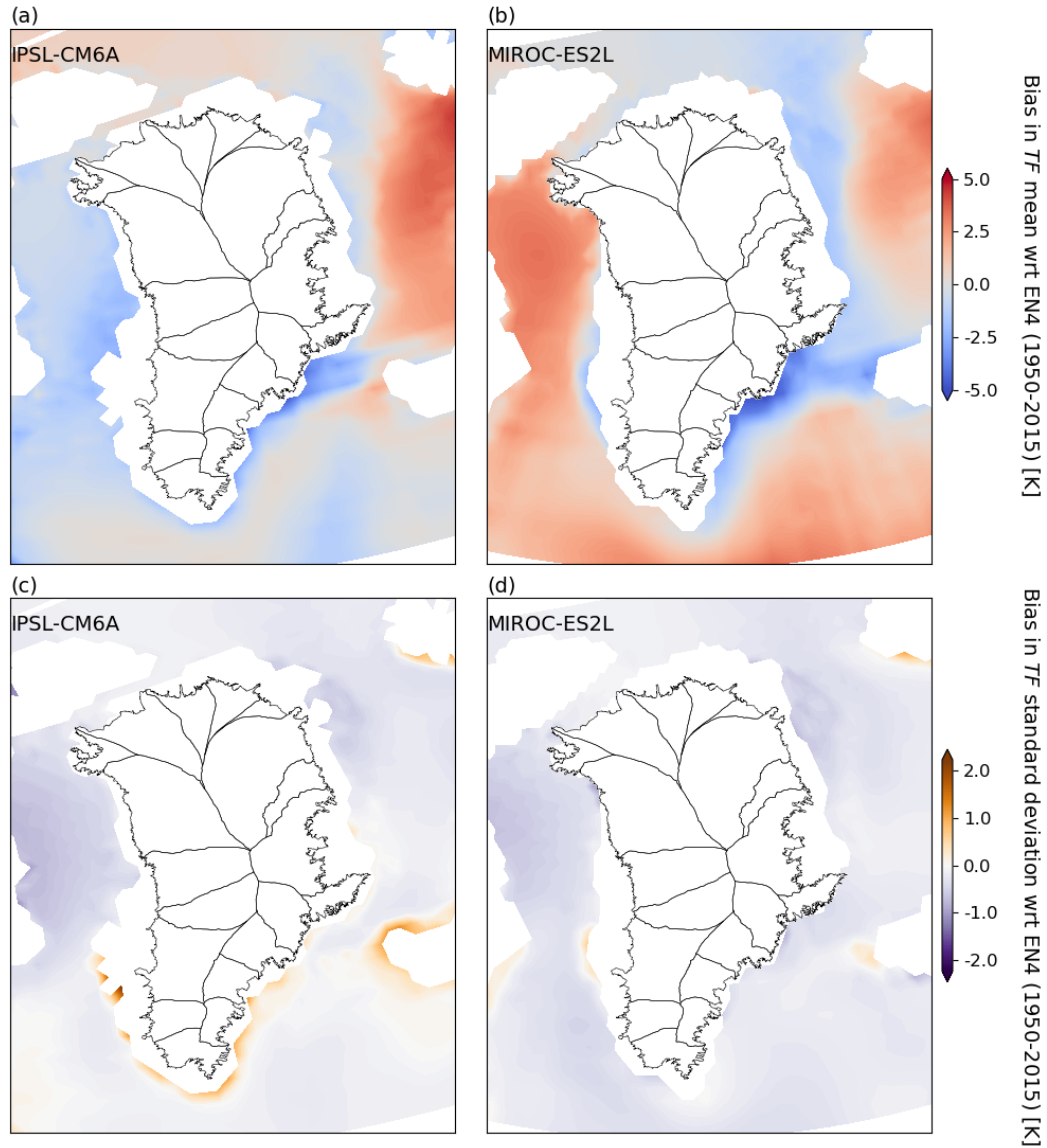


Figure 4. Bias in (a,b) mean TF and (c,d) standard deviation in TF of two AOGCMs with respect to the EN4 objective analyses (Good et al., 2013). Maps show biases of IPSL-CM6A (a,c, Boucher et al., 2020) and MIROC-ES2L (b,d, Hajima et al., 2020)

242 We use quantile mapping to correct AOGCM output, which is a method extensively
 243 used in climate and hydrological sciences (e.g., Gudmundsson et al., 2012; Themeßl et
 244 al., 2012; Cannon et al., 2015). In quantile mapping, the cumulative distribution function
 245 (CDF) of a variable from model output (any AOGCM in our case) is corrected to
 246 be equal to the CDF of the same variable from a reference dataset (EN4 in our case) over
 247 a given calibration period (1950-2015 in our case). The approach can be further extended
 248 to correct projected modeled output beyond the calibration period, using the quantile

249 delta mapping (QDM) technique developed by Cannon et al. (2015). QDM adjusts fu-
 250 ture model output by calibrating the model CDF to the reference data CDF, and by su-
 251 perimposing model-projected changes in the future period. We give here an overview of
 252 the QDM methodology, but refer to Cannon et al. (2015) for all the details. If readers
 253 need some visual intuition, we provide example results of QDM applied on time series
 254 in Figure 5.

We denote the TF from the observational dataset EN4 over the calibration period
 as TF_{obs}^{cal} with CDF F_{obs}^{cal} . The modeled TF from an AOGCM over the calibration pe-
 riod is denoted as TF_{mod}^{cal} with CDF F_{mod}^{cal} . Equalizing the model CDF to the observa-
 tional CDF is achieved by:

$$\widehat{TF}_{mod}^{cal} = [F_{obs}^{cal}]^{-1} \left[F_{mod}^{cal} \left(TF_{mod}^{cal} \right) \right], \quad (3)$$

where $[F]^{-1}$ denotes the inverse CDF. The resulting \widehat{TF}_{mod}^{cal} follows the same distribu-
 tion as F_{obs}^{cal} but preserves the relative changes as modeled by the AOGCM. In QDM,
 we also correct projected model output TF_{mod}^{proj} with CDF F_{mod}^{proj} . In this procedure, the
 first step is to calculate the nonexceedance probabilities, τ , during the projection period
 of the modeled values at each time step t :

$$\tau_{mod}^{proj}(t) = F_{mod}^{proj} \left[TF_{mod}^{proj}(t) \right], \quad (4)$$

with $\tau_{mod}^{proj}(t)$ being the probability that, when considering the full projection period, TF_{mod}^{proj}
 is less than or equal to its value at t , i.e., $TF_{mod}^{proj}(t)$. Therefore, $\tau_{mod}^{proj}(t)$ ranges between
 0 and 1. Similar to Cannon et al. (2015) we calculate the projection period CDF F_{mod}^{proj}
 over 30-year sliding windows. This approach presents the advantages of not represent-
 ing the entire projection as a single CDF, and avoiding any abrupt distributional changes
 within the projection period. The τ_{mod}^{proj} values from Eq. (4) are passed as argument to
 the inverse CDF of the calibration period, $[F_{mod}^{cal}]^{-1}$, to estimate the calibration period
 value of TF associated to them. Taking the difference between the projected model val-
 ues and their corresponding estimated calibration period values gives the estimated ab-
 solute changes in quantiles between the calibration period and the 30-year window in the
 projection period:

$$\Delta_{mod}(t) = TF_{mod}^{proj}(t) - [F_{mod}^{cal}]^{-1} \left[\tau_{mod}^{proj}(t) \right]. \quad (5)$$

The nonexceedance probability is also passed to $[F_{obs}^{cal}]^{-1}$ in order to calculate its cor-
 responding bias-corrected TF value under the observational distribution of the calibra-
 tion period:

$$\widehat{TF}_{obs:mod}^{cal:proj}(t) = [F_{obs}^{cal}]^{-1} \left[\tau_{mod}^{proj}(t) \right]. \quad (6)$$

In this manner, $\widehat{TF}_{obs:mod}^{cal:proj}(t)$ takes the statistical characteristics of the reference data dur-
 ing the calibration period. We use the physical constraint that TF cannot be below 0
 K (i.e., ocean temperature at freezing point). To enforce this constraint, we find the ob-
 servation CDF limit that corresponds to $TF = 0$ K by linearly extrapolating $[F_{obs}^{cal}]^{-1}$
 until the limit at which it yields 0 K. If $\tau_{mod}^{proj}(t)$ is below that limit, $\widehat{TF}_{obs:mod}^{cal:proj}$ is set to
 0 K. Finally, the modeled absolute change in quantiles is added back to $\widehat{TF}_{obs:mod}^{cal:proj}(t)$ to
 yield the projected bias-corrected value:

$$\widehat{TF}_{mod}^{proj}(t) = \widehat{TF}_{obs:mod}^{cal:proj}(t) + \Delta_{mod}(t). \quad (7)$$

255 Eq. (7) reintroduces the TF change signal projected by the AOGCM, $\Delta_{mod}(t)$. As such,
 256 the QDM procedure ensures that both statistical characteristics of the reference dataset,
 257 via Eq. (6), and projected changes in quantiles, via Eq. (5), are preserved. If a negative
 258 Δ_{mod} pushes $\widehat{TF}_{mod}^{proj}$ below 0 K, we set $\widehat{TF}_{mod}^{proj} = 0$ K for physical consistency.

259 In summary, the QDM technique maps the AOGCM CDF to the CDF of EN4 over
 260 the calibration period. This has the effect of reducing the biases shown in Fig. 4 to zero.
 261 However, QDM preserves the relative changes in time of TF as modeled by the AOGCMs.
 262 Finally, it allows to extend the calibration to the projection period by super-imposing
 263 the relative changes in the TF distribution that are projected by the AOGCM to the
 264 corrected TF time series.

265 2.2 Extrapolation to fjord mouths

266 The horizontal resolution of AOGCMs is insufficient to capture the dynamical pro-
 267 cesses governing ocean heat transfer from the open ocean on to the continental shelf (Slater
 268 et al., 2020; Wood et al., 2021), as these models use a typical ocean mesh of 1° (~ 75 km
 269 around Greenland). In this context, we make use of a high-resolution Arctic forward model
 270 run from the Estimating the Circulation and Climate of the Ocean (ECCO) consortium
 271 (Nguyen et al., 2012; Rignot et al., 2012). This ECCO run spans the period 1992-2009,
 272 and it has a horizontal resolution of 4 km. We use ECCO to statistically constrain the
 273 extrapolation from open ocean TF to on-the-shelf TF , close to the fjord mouths of the
 274 Greenland outlet glaciers. Note here that other high-resolution ocean model products
 275 can be used for the extrapolation (e.g., Gillard et al., 2016). Hereafter, we refer to open
 276 ocean gridpoints as offshore, and to fjord mouth gridpoints as inshore. We consider in-
 277 shore gridpoints as ECCO gridpoints closest to glacier fjord mouths, while offshore grid-
 278 points can be any other gridpoint within the 7 oceanic sectors considered (see Fig. 1a).
 279 We note that some ECCO gridpoints need to be rejected due to unphysical variability
 280 in TF , caused in general by an initialization shock (Balmaseda et al., 2009). We conser-
 281 vatively discard 2% of the gridpoints, mostly located in Eastern fjords and in the far
 282 North. The statistical extrapolation method is based on, and adapted from the work of
 283 Oliver and Holbrook (2014), as detailed in this section. A visualization of an example
 284 result of the extrapolation methodology is given in Figure 8.

285 2.2.1 Statistical relations between offshore and inshore

286 We seek a representation of inshore TF based on available offshore TF in the QDM-
 287 corrected AOGCM output. We derive offshore-inshore relationships using the high-resolution
 288 ECCO output. Inshore locations are specific to each glacier of the dataset of Wood et
 289 al. (2021) (Fig. 1a), and defined here as the 4 closest ECCO gridpoints that have a bathymetry
 290 of at least 100 m depth. Other choices could be made by applying knowledge of the re-
 291 gional dynamics, for example by selecting gridpoints along the orientation of a fjord or
 292 along contours of constant depth. The offshore locations serve as predictors in the offshore-
 293 inshore relationships, and we provide a method to optimize the choice of predictor grid-
 294 points in Section 2.2.2.

We decompose all TF (i.e., offshore, inshore, from the high-resolution ECCO, and
 from a coarse resolution AOGCM) in four different components: a mean, a trend, a sea-
 sonal cycle, and residual variability. This is expressed as:

$$TF = \overline{TF} + \dot{TF} + TF^S + TF', \quad (8)$$

295 where \overline{TF} , \dot{TF} , TF^S , and TF' denote the long-term mean, the long-term trend, the sea-
 296 sonal component, and the residual variability, respectively. We develop statistical extrap-
 297 olation relationships for the three components \overline{TF} , TF^S , and TF' . We preserve \dot{TF} un-
 298 changed from the offshore to the inshore for two reasons. First, it is questionable whether
 299 an offshore-inshore relation for the trend calculated over the period of the ECCO run
 300 (1992-2009) can be applied to AOGCM trends beyond that period. Second, while lin-
 301 ear functions represent the trend over the short 1992-2009 period well, we find evidence
 302 of quadratic trends in AOGCM simulations extending until 2100 (see Sect. 2.3). As such,
 303 any extrapolation relationship derived over 1992-2009 would not be transferable to the
 304 entire AOGCM simulation period.

First, the time-mean \overline{TF} is a scalar, for both offshore and inshore locations. As such, we can relate them linearly as:

$$\overline{TF}_{\text{in}} = \alpha \overline{TF}_{\text{off}}, \quad (9)$$

where α is the only parameter of the regression, and it is glacier-specific. The subscripts in and off denote inshore and offshore, respectively. We derive the α parameter from the ECCO relation between inshore and offshore time-mean TF :

$$\alpha = \frac{\overline{TF}_{\text{hr,in}}}{\overline{TF}_{\text{hr,off}}}, \quad (10)$$

305 where the subscript hr denotes the high-resolution ECCO model.

Second, we represent the seasonal cycle as a sum of 12 monthly effects. The monthly effect is calculated as the mean, over multiple years, of the TF anomalies, defined as the difference between the monthly value and the annual mean. For example, we compute the difference between the January TF and the annual mean TF for each year of the time series, and the January monthly effect is the mean of these anomalies. The seasonal cycle is thus represented as:

$$TF^S(t) = \sum_{i=1}^{12} M_i \delta(t, i), \quad (11)$$

where $M_{1,\dots,12}$ are the 12 monthly effects, and $\delta(t, i)$ is 1 if the time step t of the time series falls in month i , and 0 otherwise. Note that, by definition, the 12 M_i average to zero. We favor using monthly effects rather than a Fourier series, as done by Oliver and Holbrook (2014), because the latter approach does not capture well the 0 K lower bound on TF , which can be important at high latitudes. Similarly to our approach for \overline{TF} , we relate the inshore and offshore monthly effects linearly for each month:

$$M_{i,\text{in}} = \gamma M_{i,\text{off}}. \quad (12)$$

The linear scaling factor γ is calibrated with the high-resolution ECCO product:

$$\gamma = \frac{\sum_{i=1}^{12} |M_{i,\text{hr,in}}|}{\sum_{i=1}^{12} |M_{i,\text{hr,off}}|}, \quad (13)$$

306 and γ thus captures how strongly seasonality is amplified or reduced inshore compared
 307 to offshore. We calculate a single γ with the absolute values of all 12 monthly effects rather
 308 than having a specific γ for each individual month, because individual M_i values close
 309 to zero could make the ratio unphysically large.

Finally, after subtracting the mean, the trend, and seasonality components from the TF time series, only the non-seasonal residual variability TF' remains (Eq. (8)). We apply a statistical relationship between offshore and inshore TF' . We relate the standard deviations of the inshore and offshore variability linearly:

$$\sigma [TF'_{\text{in}}(t)] = \beta \sigma [TF'_{\text{off}}(t)], \quad (14)$$

where $\sigma []$ denotes the standard deviation of the time series in the brackets. We estimate the β parameter from the ratio of ECCO standard deviations in inshore and offshore residual variability:

$$\beta = \frac{\sigma [TF'_{\text{hr,in}}(t)]}{\sigma [TF'_{\text{hr,off}}(t)]}. \quad (15)$$

310 If the trend \dot{TF} is not removed, it would be included in TF' , causing β to be inflated or
 311 deflated if offshore and inshore trends differ. By detrending, we thus ensure that β cap-
 312 tures the ratio of residual inter-annual variability in TF instead of longer-term tenden-
 313 cies.

314 Using the calibrated statistical relationships, we construct an estimate of inshore
 315 TF of a coarse-resolution AOGCM using its offshore TF as a predictor. In other words,

316 we can use $TF_{cr,off}$ to predict $TF_{cr,in}$, where the subscript cr denotes a coarse-resolution
 317 AOGCM. We predict the three extrapolated components of $TF_{cr,in}$ separately:

$$\begin{cases} \overline{TF}_{cr,in} = \alpha \overline{TF}_{cr,off} \\ TF_{cr,in}^S(t) = \gamma \sum_{i=1}^{12} M_{i,cr,off} \delta(t, i) \\ TF'_{cr,in}(t) = \beta TF'_{cr,off}(t) \end{cases} \quad (16)$$

318 By multiplying $TF'_{cr,off}$ by β , we use the fact that the residuals have mean zero by con-
 319 struction, and we assume that they follow a normal distribution. As such, $TF'_{cr,in}$ fol-
 320 lows a normal distribution with mean zero and its standard deviation is $\beta\sigma(TF'_{cr,off})$.
 321 Our Eqs. (14) and (15) differ from the approach of Oliver and Holbrook (2014), as they
 322 related $TF'_{hr,off}$ and $TF'_{hr,in}$ by linear regression to estimate β . By using the ratio of
 323 the standard deviations instead, we avoid issues of decreased variability in $TF'_{cr,in}$ com-
 324 pared to $TF'_{cr,off}$ when $TF'_{hr,in}$ and $TF'_{hr,off}$ show similar variability, but are not well-
 325 correlated in time. However, our approach relies on the assumption of normally-distributed
 326 residuals. To verify this assumption, we draw 1000 random bootstrap samples of size 50
 327 from all the monthly values of residual variability, and compute the Shapiro-Wilk nor-
 328 mality test (Shapiro & Wilk, 1965). We find that the normality assumption is validated
 329 for 87% of these bootstrap samples at the 5% significance level.

Using Eqs. (8) and (16), the full estimated time series of $TF_{cr,in}$ is reconstructed
 as:

$$TF_{cr,in} = \overline{TF}_{cr,in} + \dot{TF}_{cr,off} + TF_{cr,in}^S + TF'_{cr,in}. \quad (17)$$

330 Note that the trend is preserved from the offshore AOGCM gridpoint. Because the ex-
 331 trapolation is based on the short period of ECCO output (1992-2009), we simply remove
 332 a linear trend for the extrapolation process, as a higher-order polynomial would likely
 333 include part of the residual variability which we aim to extrapolate.

334 For a given glacier front (i.e., a given inshore location), we need to determine an
 335 optimal offshore predictor gridpoint of the coarse-resolution AOGCM (see Sect. 2.2.2).
 336 However, the parameters α , γ , and β are constrained with relations from ECCO. Thus,
 337 once the AOGCM offshore gridpoint predictor is determined, we find its nearest-neighbor
 338 ECCO gridpoint. We relate the $TF_{hr,off}$ of this ECCO gridpoint to the ECCO $TF_{hr,in}$
 339 of the glacier front to constrain the parameters. As a reminder, $TF_{hr,in}$ for a given glacier
 340 front is computed as the average of the 4 ECCO gridpoints closest to the glacier front.

341 2.2.2 Determining the offshore predictor locations

342 In this section, we describe a procedure, modified from Oliver and Holbrook (2014),
 343 to determine an optimal offshore gridpoint as a predictor for the inshore AOGCM TF
 344 time series of a given glacier front. We limit the possible domain for an offshore predic-
 345 tor to our 7 oceanic sectors around Greenland (Fig.1a). To determine the optimal pre-
 346 dictors, we use three quantitative criteria for each TF component.

The first criterion is a quality function, Q . The quality function is defined as the
 agreement between the QDM-corrected coarse-resolution AOGCM and the high-resolution
 ECCO. The quality is defined separately for each component:

$$\overline{Q} = \frac{|\overline{TF}_{cr,off} - \overline{TF}_{hr,off}|^{-1}}{1 + |\overline{TF}_{cr,off} - \overline{TF}_{hr,off}|^{-1}}, \quad (18)$$

$$Q^S = \left[\frac{1 + r(TF_{cr,off}^S, TF_{hr,off}^S)}{2} \times \min \left(\frac{\sum_{i=1}^{12} |M_{i,cr,off}|}{\sum_{i=1}^{12} |M_{i,hr,off}|}, \frac{\sum_{i=1}^{12} |M_{i,hr,off}|}{\sum_{i=1}^{12} |M_{i,cr,off}|} \right) \right]^{1/2}, \quad (19)$$

$$Q' = \left[\frac{1 + r(TF'_{cr,off}, TF'_{hr,off})}{2} \times \min \left(\frac{\sigma(TF'_{cr,off})}{\sigma(TF'_{hr,off})}, \frac{\sigma(TF'_{hr,off})}{\sigma(TF'_{cr,off})} \right) \right]^{1/2}, \quad (20)$$

347 where $r(\cdot)$ denotes the correlation coefficient. Our expressions for the quality functions
 348 slightly differ from those of Oliver and Holbrook (2014). Note that Eq. (18) avoids ex-
 349 treme values of \bar{Q} in the case of \overline{TF} being close to zero, while the expressions of Eqs. (18,
 350 19, 20) all ensure that \bar{Q} , Q^S , and Q' remain bounded between 0 and 1. By using the
 351 quality functions as a criterion for selecting the offshore predictor gridpoint of the coarse-
 352 resolution AOGCM, we favor offshore gridpoints where the QDM-corrected AOGCM agrees
 353 well with ECCO. The two terms in Eq. (19) favor strong temporal correlation between
 354 the seasonality patterns of ECCO and the AOGCM and similar total seasonal amplitude,
 355 respectively. Similarly, the two terms in Eq. (20) favor temporal correlation between and
 356 similar variability amplitude of the residuals of ECCO and the AOGCM. In Eqs. (19,
 357 20), we give equal weights to the correlation and amplitude terms by taking their geo-
 358 metric mean.

The second criterion is a strength function, S . The strength functions measure the
 similarity between the offshore TF components to their corresponding components of
 the inshore gridpoint of interest in the high-resolution model ECCO. We compute the
 strength functions at all the ECCO gridpoints that are a nearest neighbor of an exist-
 ing AOGCM gridpoint. In this manner, each nearest neighbor is attributed a strength
 criterion value. In other words, the values of the strength functions of a given coarse-
 resolution AOGCM gridpoint depend on the TF time series of the nearest-neighbor high-
 resolution ECCO model gridpoint. The expressions for the strength functions are similar
 to those of the quality functions, and are also defined separately for each component:

$$\bar{S} = \frac{|\overline{TF}_{hr,off} - \overline{TF}_{hr,in}|^{-1}}{1 + |\overline{TF}_{hr,off} - \overline{TF}_{hr,in}|^{-1}}, \quad (21)$$

$$S^S = \left[\frac{1 + r(TF_{hr,off}^S, TF_{hr,in}^S)}{2} \times \min \left(\frac{\sum_{i=1}^{12} |M_{i,hr,off}|}{\sum_{i=1}^{12} |M_{i,hr,in}|}, \frac{\sum_{i=1}^{12} |M_{i,hr,in}|}{\sum_{i=1}^{12} |M_{i,hr,off}|} \right) \right]^{1/2}, \quad (22)$$

$$S' = \left[\frac{1 + r(TF'_{hr,off}, TF'_{hr,in})}{2} \times \min \left(\frac{\sigma(TF'_{hr,off})}{\sigma(TF'_{hr,in})}, \frac{\sigma(TF'_{hr,in})}{\sigma(TF'_{hr,off})} \right) \right]^{1/2}. \quad (23)$$

359 Strength functions thus attribute more weight to offshore gridpoints where ECCO es-
 360 timates that a given TF component is similar to the inshore TF component close to the
 361 glacier front.

The last criterion is a simple localization function, L . It is formulated as an isotropic
 two-dimensional Gaussian function centered on the inshore location (x_{in}, y_{in}) . The lo-
 calization function attributes more weight to offshore gridpoints closer to the inshore lo-
 cation, and it is the same for the three TF components:

$$L = \exp \left[- \frac{\left((x_{off} - x_{in})^2 + (y_{off} - y_{in})^2 \right)}{2\lambda_L^2} \right], \quad (24)$$

362 where λ_L is an isotropic decay lengthscale. We set $\lambda_L = 600$ km. This is chosen because
 363 the mean correlation between TF time-series within a given radius in ECCO falls be-
 364 low 0.7 for a radius above 600 km, when considering the 7 oceanic sectors around Green-
 365 land (Fig.1a). However, the decay lengthscale can be adjusted depending on the impor-
 366 tance attributed to keeping offshore predictors close to the inshore location. Furthermore,
 367 Eq. (24) can easily be converted to an anisotropic function, with different decay scales
 368 in the zonal and meridional directions.

The functions Q , S , and L are combined into a single cost function J . In this pro-
 cess, one can use different weights ranging between 0 and 1 for the three functions, w_Q ,
 w_S , and w_L ,

$$J = \frac{1}{(1 - w_Q + w_Q Q)(1 - w_S + w_S S)(1 - w_L + w_L L)}, \quad (25)$$

369 and there is one cost function J per TF component. Here, we make the simplest choice
 370 of equally-weighted functions, with $(w_Q, w_S, w_L) = (1,1,1)$. While Oliver and Holbrook
 371 (2014) used a different predictor gridpoint per TF component, we find that the spatial
 372 differences between the cost functions of the different TF components are minor. Thus,
 373 for simplicity, we compute the total cost J_T as the average of the cost functions of the
 374 three components. The gridpoint minimizing J_T is used as the offshore gridpoint pre-
 375 dictor. We provide examples of the searching method for the optimal offshore predic-
 376 tor gridpoint in Sect. 3.2. We use the optimal offshore predictor to construct a synthetic
 377 inshore TF time series following the method described in Sect. 2.2.1.

378 2.3 Fitting of statistical models

379 The QDM-corrected and inshore-extrapolated TF time series are entirely deter-
 380 ministic, but our goal is also to generate many TF time series that represent realizations
 381 of internal climate variability. Therefore, we calibrate statistical time series models to
 382 the deterministic time series, and use a stochastic term to represent residual variability
 383 in TF . Here, we consider output from two different AOGCMs, under two possible emis-
 384 sion scenarios, and at 226 Greenland marine glaciers. Each combination of AOGCM and
 385 emission scenario has a given number of ensemble members. The ensemble members dif-
 386 fer due to minor differences in the initial conditions, which can amplify during the AOGCM
 387 simulation owing to the sensitive dependence on initial conditions of the climate system
 388 (Hasselmann, 1976; Kay et al., 2015; Maher et al., 2019). For each individual glacier, the
 389 number of TF time series available from a given AOGCM under a specific emission sce-
 390 nario is limited by the number of ensemble members. Because AOGCMs are computa-
 391 tionally expensive models, the number of members is in general of the order 1 to 10 for
 392 CMIP6 experiments until 2100. Statistical samples of such sizes of TF time series are
 393 thus too small to fully characterize the distribution of possible oceanic conditions affect-
 394 ing Greenland glaciers in the future. The statistical models that we develop here must
 395 (i) be representative of the deterministic inshore series, (ii) account for internal climate
 396 variability using a stochastic parameterization, and (iii) efficiently generate a large num-
 397 ber of TF time series at low computational expense. Each statistical model is specific
 398 to a combination of AOGCM, emission scenario, and glacier. We detail their implemen-
 399 tation in this section.

At a given inshore location, we process all the TF time series in the same manner
 (Eq. (8)). First, we decompose each series in a mean, a trend, a seasonality, and a resid-
 ual component. In contrast to the procedure in the extrapolation process (Sect. 2.2.1),
 time series here are considered over the entire AOGCM run (1850-2100) and not only
 over their overlapping period with ECCO (1992-2009). For this reason, we estimate the
 sum of mean and trend components as a piecewise polynomial function with a break-
 point at date t_{brk} . We use a second-order polynomial, because it captures the non-linear
 warming trend by the end of the century in high-emission scenarios. Mathematically, the
 mean-plus-trend component that we estimate corresponds to:

$$\begin{cases} \overline{TF} + TF(t) = a_0^{pre} + a_1^{pre}(t - t_0) + a_2^{pre}(t - t_0)^2 & \text{if } t \leq t_{brk} \\ \overline{TF} + TF(t) = a_0^{post} + a_1^{post}(t - t_{brk}) + a_2^{post}(t - t_{brk})^2 & \text{if } t > t_{brk} \end{cases}, \quad (26)$$

400 where t_0 is the initial date of the time series. The breakpoint t_{brk} is not fixed but varies
 401 between different TF time series to optimize the fit of Eq. (26). The *pre* and *post* su-
 402 perscripts denote coefficients applying before and after the breakpoint t_{brk} , respectively.
 403 Ensemble members of a same AOGCM agree relatively well on general trends at the cen-
 404 tennial time scale (Maher et al., 2019). For this reason, our method does not attribute
 405 internal variability to the mean-plus-trend component, which we take as entirely deter-
 406 ministic.

The seasonality is still evaluated as 12 monthly effects (Eq. (11)). However, we ob-
 serve that seasonality in TF strongly increases by 2100 in high-emission scenarios, both

in raw AOGCM output and in our QDM-corrected inshore-extrapolated time series. For this reason, over the period 1850-2100, we represent each monthly effect M_i as a piecewise linear function with a breakpoint fixed at 2015:

$$\begin{cases} M_i(t) = b_0^{pre} + b_1^{pre}(t - t_0) & \text{if } t \leq 2015, \text{ for } i = 1, \dots, 12 \\ M_i(t) = b_0^{post} + b_1^{post}(t - 2015) & \text{if } t > 2015, \text{ for } i = 1, \dots, 12 \end{cases} \quad (27)$$

407 and all the M_i values can be used to calculate the seasonal component (Eq. (11)). As-
 408 suming a single breakpoint avoids having different optimal breakpoints for different months,
 409 which would complicate the representation of seasonality. Here, we elect 2015 as the break-
 410 point because it is the transition between historical and prediction simulations of AOGCMs
 411 in the CMIP6 protocol. Finally, after removing the mean-plus-trend component (using
 412 Eq. (26)), and the seasonality component (using Eq. (27)) from a given TF series, we
 413 treat the remaining signal as the residual component, TF' .

The residual component is modeled as an autoregressive-moving-average (ARMA) process on an annual time scale. ARMA models have been principally popularized by Box and Jenkins (1976), and are extensively used in geophysical sciences to represent dynamical processes that exhibit memory (Storch & Zwiers, 1999; Mudelsee, 2010; Wilks, 2011). Their advantage is the ability to represent a large range of temporal autocorrelation features, while using only a small number of parameters. ARMA processes have been used previously to represent ocean temperatures and their residuals (e.g., Hasselmann, 1976; Hausfather et al., 2017; Cheng et al., 2022). It is important to remove the general trend, as well as the trend in monthly effects to ensure stationarity of the residual component time series, i.e., the residuals should not exhibit a trend or changing variability over time. By modeling the residual component as an ARMA process, our goal is to capture the different time scales of variability in oceanic conditions around Greenland, ranging from inter-annual to multi-decadal variability (Straneo & Heimbach, 2013). This temporal complexity is partly driven by the influence of the North Atlantic Oscillation and the Atlantic Multi-decadal Oscillation on variability in waters of both Polar and Atlantic origins (Dickson et al., 2000; Rignot et al., 2012). An ARMA model of autoregressive (AR) order p and moving-average (MA) order q , denoted ARMA(p,q), for a generic variable y is formulated as:

$$y_t = \sum_{i=1}^p \varphi_i y_{t-i} + \sum_{j=1}^q \theta_j \epsilon_{t-j} + \epsilon_t, \quad (28)$$

where the $\varphi_1, \dots, \varphi_p$ are the AR coefficients, and the $\theta_1, \dots, \theta_q$ are the MA coefficients. The ϵ_t term is a Gaussian noise term. In an ARMA model, the φ_i coefficients capture the memory of the process, and the θ_i coefficients represent the persistence of random noise effects in the system. In our specific case, ϵ_t allows us to prescribe covariance between different glaciers by being randomly sampled from a multivariate Gaussian of which the covariance matrix has dimensions equal to the total number of glacier front locations (i.e., 226). From this multivariate Gaussian, one can sample a random vector ϵ_t of size equal to the number of glaciers, and which consists of the individual ϵ_t applied at each glacier front:

$$\epsilon_t \sim N(0, \Sigma). \quad (29)$$

For each of the TF' time series (i.e., the residual variability), we calibrate all possible combinations of ARMA models of both AR orders (p) and MA orders (q) ranging from 0 to 4. For each possible ARMA(p,q) calibrated model, we evaluate its Bayesian Information Criterion (BIC) (Schwarz, 1978). In fitting a statistical model to data, the BIC measures the likelihood of the model, but penalizes the number of parameters used in the model. Its purpose is to find the adequate balance between model fit and model complexity, thus avoiding overfitting. It is calculated as:

$$\text{BIC} = m \ln(n) - 2 \ln(\hat{L}), \quad (30)$$

414 where m is the total number of parameters, n is the number of data points, and \hat{L} is the
 415 value of the likelihood function evaluated with the calibrated model. In our case, $m =$
 416 $p+q$ and $n = 250$ (i.e., number of yearly residual values in a 1850-2100 time series). For
 417 a given glacier, emission scenario, and AOGCM, there is one combination of (p,q) min-
 418 imizing the BIC per individual ensemble member. To decide which of all these poten-
 419 tial best-fitting ARMA models we use, we take the most favored (p,q) combination among
 420 the selected (p,q) combinations for the different members, and denote this preferred com-
 421 bination as (p^*,q^*) . In case of a tie among the selected models, we take the one of lower
 422 order (i.e., lower $p+q$). As such, for a given glacier, emission scenario, and AOGCM,
 423 we have a single ARMA(p^*,q^*) model representative of the residuals. To calibrate the
 424 φ_i coefficients, θ_j coefficients, and the marginal variance of ϵ_t (see Eq.(28)), we fit all the
 425 ensemble member time series with the (p^*,q^*) combination. We take the average of the
 426 φ_i , θ_j , and marginal variance values across the ARMA(p^*,q^*) models of all the ensem-
 427 ble members. This averaging procedure is equivalent to considering the parameter val-
 428 ues from the different ensemble members as a sample of the true population of AOGCM
 429 parameter values. As per the central limit theorem, the average parameter values are
 430 thus asymptotically representative of a mean AOGCM simulation. This procedure is re-
 431 peated for each combination of glacier, AOGCM, and emission scenario. The calibrated
 432 ARMA(p^*,q^*) model allows us to generate a large set of time series at a given glacier,
 433 representative of the TF' residuals modeled by the corresponding AOGCM under the
 434 forcing of the corresponding emission scenario.

435 The long-term mean and trend (Eq. (26)) and monthly effects (Eq. (27)) in TF
 436 are taken from the across-members AOGCM ensemble mean at each glacier and for each
 437 emission scenario. These ensemble mean deterministic components can be added to an
 438 ARMA-generated stochastic TF' residuals time series to produce a TF time series.

We can account for inter-glacier covariability when generating the ϵ_t , as highlighted
 by Eq. (29). In other words, the calibrated marginal variances are used to fill the diag-
 onal entries of the covariance matrix, but the off-diagonal entries can be estimated from
 the empirical correlation of the TF' time series of a same member at all the glacier front
 locations. Because the number of values to be estimated in the covariance matrix is very
 large compared to the number of yearly samples of TF' , it is preferable to compute a sparse
 correlation matrix instead of relying on the empirical correlation matrix (e.g., Hu & Cas-
 truccio, 2021). We employ the commonly-used graphical lasso method to compute a sparse
 correlation matrix \hat{C}_i for the i th ensemble member (Friedman et al., 2008). We average
 the \hat{C}_i across all the ensemble members to yield an estimated correlation matrix \hat{C} for
 a combination AOGCM-emission scenario. From \hat{C} and the diagonal matrix of the in-
 dividual calibrated marginal variances at all the glacier front locations, \bar{K} , we compute
 the sparse covariance matrix $\hat{\Sigma}$:

$$\hat{\Sigma} = \bar{K}^{\frac{1}{2}} \hat{C} \bar{K}^{\frac{1}{2}}, \quad (31)$$

439 and $\hat{\Sigma}$ is used as the covariance matrix for generating random TF' realizations across
 440 all the glaciers, following Eqs. (28, 29). As a reminder, $\hat{\Sigma}$ is specific to a given AOGCM-
 441 emission scenario configuration, is an average across all the ensemble members, and cap-
 442 tures covariance between TF' at all the glacier front locations. In the Results section,
 443 Figure 15 gives a visual intuition for the difference between an empirical and a sparse
 444 correlation matrix.

445 To summarize, the stochastic time series models described in this subsection pro-
 446 vide a computationally efficient way to generate time series of variability in TF . The pa-
 447 rameters of the models are calibrated to the temporal variability characteristics of the
 448 deterministic QDM-corrected and inshore-extrapolated AOGCM TF time series. In ad-
 449 dition, the time series models can represent spatial covariance in TF . This latter aspect
 450 is critical when evaluating the response to oceanic forcing of the Greenland ice sheet as
 451 a whole, instead of on a glacier-by-glacier basis.

3 Results

To illustrate our method, we use outputs from two AOGCMs that took part in CMIP6. The AOGCMs chosen for this study are MIROC-ES2L (Hajima et al., 2020) and IPSL-CM6A (Boucher et al., 2020), as these models are updated versions of two of the AOGCMs used in the ISMIP6 Greenland intercomparison (Goelzer et al., 2020). However, the method outlined in Sect. 2 is applicable to any AOGCM. We consider both AOGCMs in a low- and a high-emission scenario: ssp126 and ssp585, respectively. The forcing scenarios cover the period 2015-2100, and are preceded by the AOGCM historical runs over 1850-2015. Note here that we only use the 1950-2015 period as calibration period, because it overlaps the historical AOGCM run and the period of high observational weight values in EN4 (Fig. 3). Under these emission scenarios, MIROC-ES2L and IPSL-CM6A have 10 and 5 ensemble members, respectively. Finally, we investigate TF conditions at the 226 outlet glaciers with marine termini (Wood et al., 2021) (see Fig. 1a). In total, our analysis involves 6780 TF time series.

3.1 Quantile Delta Mapping results

In this section, we illustrate and evaluate the QDM approach described in Section 2.1. Figure 5 shows examples of the QDM application at two different locations using member r1 of MIROC-ES2L. In Figure 5a, the raw AOGCM TF shows a positive bias of ~ 3 K, and an underestimation of temporal variability with respect to EN4. After QDM, these differences are corrected, while the features of relative changes and future trends in the raw AOGCM output are preserved. In contrast, in Figure 5b, the AOGCM is in good agreement with EN4, both for the mean and the amplitude of variability. As such, the QDM-corrected TF time series remains similar to the raw time series.

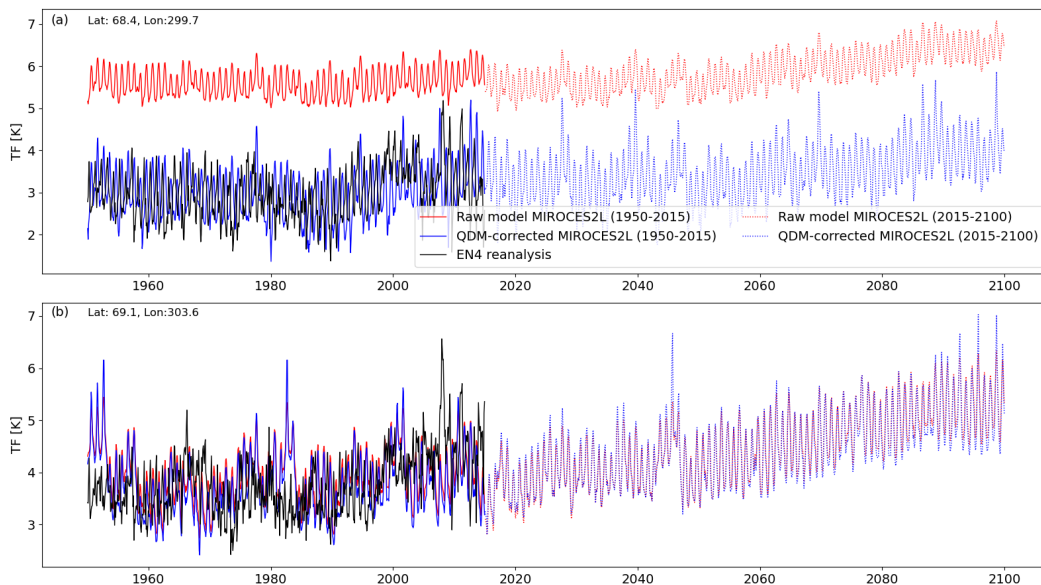


Figure 5. TF time series for Member r1 of ssp585 experiment from MIROC-ES2L at two different locations (a and b, at fa and fb in Fig. (1b)). QDM is applied on the raw MIROC-ES2L TF time series using the TF time series of the EN4 nearest neighbor gridpoint. The black line shows the EN4 nearest neighbor TF time series. Red lines show the TF time series from MIROC-ES2L. Blue lines show TF time series of the MIROC-ES2L after QDM correction. Dotted lines show the projection of the MIROC-ES2L TF time series beyond the calibration period (1950-2015). The two locations are chosen for illustrative purposes.

475 In order to validate the QDM method, we evaluate the direct match between modeled TF pre- and post-QDM correction with TF from in-situ CTD profile data. We use
 476 raw CTD profile data available from the EN4 dataset (Good et al., 2013). Because CTD
 477 profile data are used as a constraint in the EN4 objective analyses, they cannot serve
 478 as independent data to evaluate the improvement in model fidelity with respect to ob-
 479 servations after QDM correction. For this reason, we perform a second QDM calibration
 480 with only a subset of the calibration period: 1950-2000 instead of 1950-2015. The
 481 CTD data from the period 2000-2015 is subsequently used to evaluate the models after
 482 the QDM procedure was applied over this reduced 1950-2000 calibration period. In this
 483 way, the EN4 objective analyses used for the QDM-correction are independent of the raw
 484 CTD data used for the model evaluation. We compute summary statistics for the agree-
 485 ment between TF from the CTD profile observations with the raw AOGCM TF and with
 486 the QDM-corrected AOGCM TF . Specifically, from the EN4 dataset, we take all the CTD
 487 profile data within the 7 oceanic sectors outlined in Figure 1a, extending at least until
 488 500 m depth, and falling into the period 2000-2015. For each individual CTD profile, we
 489 find the nearest AOGCM gridpoint, and compute its TF at the time step closest to the
 490 CTD collection date. MIROC-ES2L and IPSL-CM6A have 10 and 5 members, respec-
 491 tively. Because there are 17 390 CTD profiles fulfilling our conditions, this results in 173
 492 900 and 86 950 pairwise comparisons of modeled versus observed TF for MIROC-ES2L
 493 and IPSL-CM6A, respectively. The pairwise comparisons and summary statistics are shown
 494 in Figure 6. For MIROC-ES2L, the QDM correction reduces the bias magnitude by 42%.
 495 The Root Mean Squared Error (RMSE) is reduced by 29% and the proportion of vari-
 496 ance explained (R^2) improves from 0.62 to 0.78. For IPSL-CM6A, the negative bias is
 497 amplified after the QDM correction from -0.11 to -0.29 K. However, the RMSE decreases
 498 by 24% and R^2 increases from 0.63 to 0.83. These results show that, even in a case where
 499 calibration is performed only using the EN4 objective analyses over 1950-2000, QDM im-
 500 proves the agreement of AOGCMs TF with respect to 2000-2015 CTD profiles.
 501

502 3.2 Extrapolation results

503 For each inshore location, our method selects one offshore predictor location by min-
 504 imizing the average cost function (Eq. (25)) for the mean (\overline{TF}), seasonality (TF^S), and
 505 residual variability (TF^V) components (see Section 2.2.2). As an example of offshore pre-
 506 dictors selection, we show some total cost functions, J_T , for member r1 of IPSL-CM6A.
 507 We show J_T for three of the largest Greenland outlet glaciers, and situated in geograph-
 508 ically distinct areas: Helheim glacier in the South-East (Fig. 7a), Sermeq Kujalleq (also
 509 called Jakobshavn Isbræ) in the Central-West (Fig. 7b), and Petermann glacier in the
 510 North (Fig. 7c) (see also Fig. 1b for the glacier locations). For Helheim glacier, the pre-
 511 predictor location is further North, upstream along the East Greenland Current (Fig. 1b).
 512 This current, originating at about 80° North and flowing southward, provides a phys-
 513 ical connection to the offshore predictor (Strass et al., 1993). In this case, this location
 514 is preferred to closer gridpoints because of stronger discrepancies of the AOGCM with
 515 respect to ECCO close to the coast. The predictor location of Sermeq Kujalleq shows
 516 the shortcoming of the bathymetry used by coarse-resolution AOGCMs: the extent of
 517 the white areas in the map shows where ocean depth is less than 100 m in the AOGCM,
 518 whereas ECCO can simulate ocean dynamics up to the fjord mouth (see Fig. 1b). Fi-
 519 nally, the predictor for Petermann glacier shows that predictability for TF in the North-
 520 ern most latitudes is very low for the rest of the ocean around Greenland. The limit be-
 521 tween low- and high-predictability areas is likely attributable to the location of the south-
 522 ern edge of sea-ice in winter and to the respective influences of Atlantic and Arctic wa-
 523 ters (Straneo et al., 2022).

524 For the same member r1 of IPSL-CM6A, we show the time series resulting from
 525 the inshore extrapolation process at Helheim glacier in Figure 8. In this particular case,
 526 the extrapolation results in a cooler inshore mean, and enhanced seasonality and resid-
 527 ual variability. Figure 9 shows the effect of the extrapolation for all the members of the

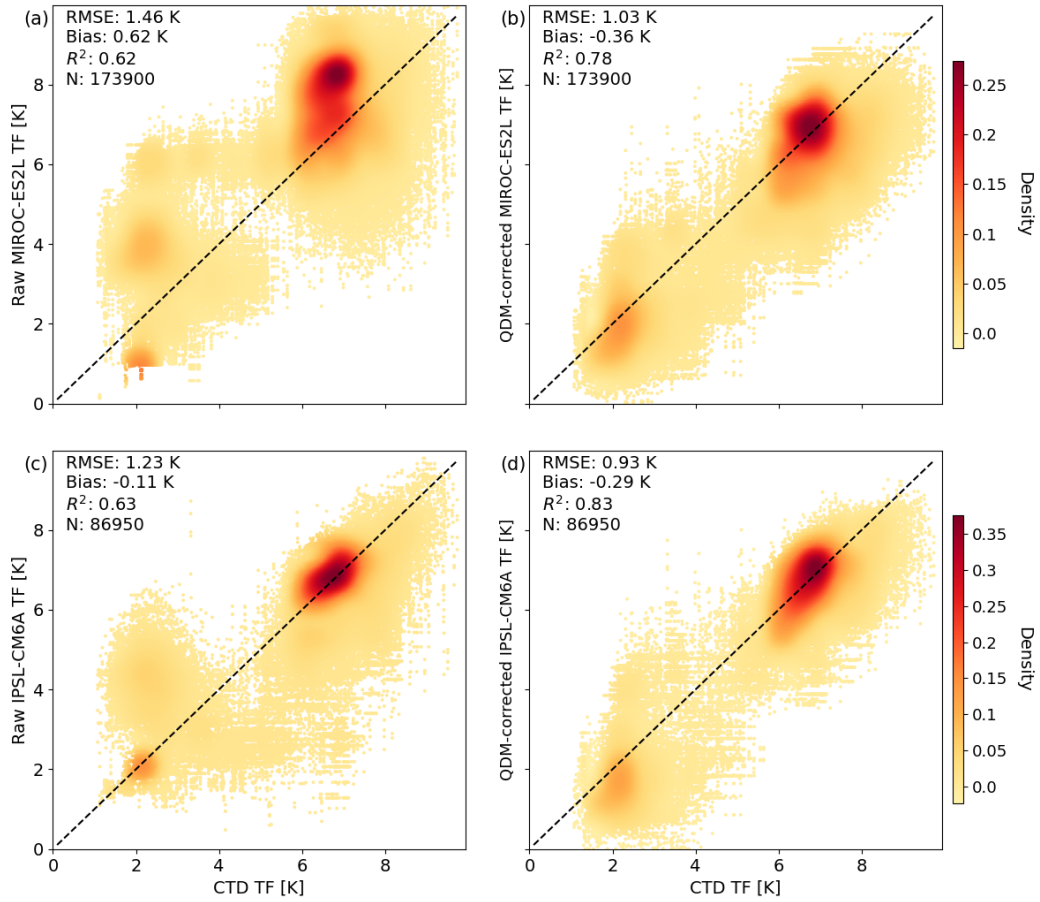


Figure 6. Comparison of raw AOGCM TF (a, c) and QDM-corrected AOGCM TF (b, d) with in-situ CTD profile data. For the purpose of evaluation, the calibration period is limited to 1950-2000, and the fit statistics are evaluated with respect to CTD data from 2000-2015 only. Evaluation is performed for MIROC-ES2L (a, b) and IPSL-CM6A (c, d). RMSE, R^2 , and N denote root mean squared error, coefficient of determination, and total number of pairwise comparisons, respectively.

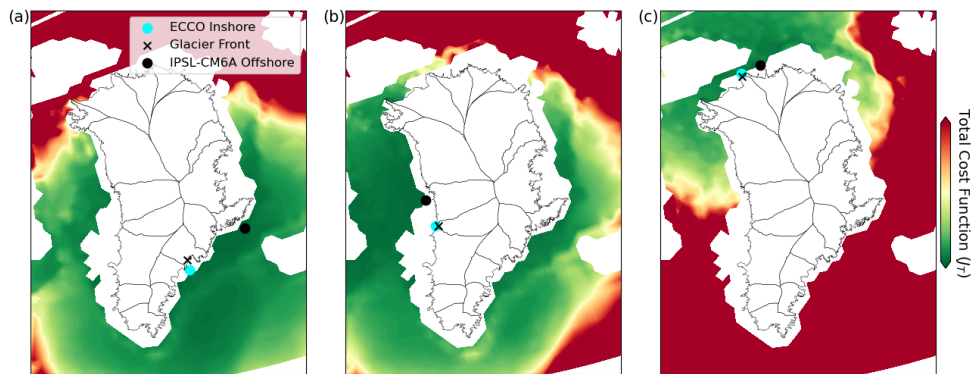


Figure 7. Optimal offshore predictors for r1 member of the IPSL-CM6A AOGCM. Shown at Helheim glacier (a), Sermeq Kujalleq (b), and Petermann glacier (c).

528 two AOGCMs in both emission scenarios and for all glaciers. Figure 9a shows boxplots
 529 of three parameters: (i) α , the inshore-to-offshore ratio in mean TF (\overline{TF}) (see Eq. (10)),
 530 (ii) γ , the inshore-to-offshore ratio in the total amplitude of the monthly effects in TF
 531 (see Eq. (13)), and (iii) β the inshore-to-offshore ratio in the standard deviation of the
 532 residual variability in TF (TF') (see Eq. (15)).

533 The parameter α has a mean of 0.84, and an inter-quartile range of [0.75;0.99] (Fig.
 534 9a). \overline{TF} is thus, on average, slightly reduced from the offshore to the inshore. Potential
 535 physical causes are (i) shallower bathymetry blocking access to warm Atlantic Waters,
 536 (ii) Arctic Waters being carried along the coast via the East Greenland Coastal Current
 537 and, subsequently, via the West Greenland Current (Fig. 1b), (iii) vertical mixing during
 538 the transit from the shelf towards the glacier, and (iv) the cooling effect of freshwa-
 539 ter discharge from the ice sheet (Buch, 2002).

540 The ratio in amplitude of monthly effects between inshore and offshore derived from
 541 ECCO (γ) spans a larger range of values (Fig. 9a). The median (1.10) and mean (1.11)
 542 show that the distribution of γ is approximately centered around 1. However, the dis-
 543 tribution is characterized by a high number of outliers in both the lower- and upper-end,
 544 with minimum and maximum values of 0.17 and 2.94, respectively. This large range of
 545 values suggests that processes influencing differences between offshore and inshore sea-
 546 sonal amplitude vary between geographical regions. This is illustrated by the map of sea-
 547 sonal amplitude in ECCO, which we approximate as half the difference between max-
 548 imum and minimum monthly effects (Fig. 10a). In the South-East, Central-East, and
 549 South-West basins, seasonal amplitude inshore is substantially larger. On the other hand,
 550 the difference between offshore and inshore amplitude is small in the Central-West, North-
 551 West, North, and North-East basins. These between-regions differences explain the large
 552 range of γ .

553 Finally, the β parameter is closely centered around 1 (Fig. 9a, mean=0.99, median=1.01),
 554 with no strong outlier. Figure 10b shows that ECCO residual variability (TF') is larger
 555 closer to the coast, which should favor β values larger than 1. The reason for β remain-
 556 ing close to 1 is that offshore predictors are generally located close to the inshore loca-
 557 tion, as the examples in Figure 7 show. As such, inshore locations and offshore predic-
 558 tor locations have, on average, equal standard deviation in residual variability in ECCO.

559 3.3 Statistical models of the residual component

560 Our procedure for isolating the residual variability by removing the trend and sea-
 561 sonality components (Eqs. (26),(27)) effectively renders the TF' time series stationary.
 562 This is validated as the null hypothesis of non-stationarity in the Augmented Dickey Fuller
 563 test (Dickey & Fuller, 1981) is rejected with significance for all the 6780 TF' time se-
 564 ries (p-values<0.05). For each TF' time series, we calibrate ARMA models (Eq. (28))
 565 and select the best-fitting ARMA model by minimizing the BIC (Eq. (30)) among the
 566 models tested (see Sect. 2.3). Histograms in Figure 11 show the optimal (p,q) orders se-
 567 lected. Our procedure finds that, in general, low order ARMA models fit the TF' time
 568 series best. An autoregressive order of 1 (i.e., $p = 1$) is selected for 51 % of the cases,
 569 and more specifically an ARMA(1,0) (i.e., AR(1)) for 42 % of the cases. None of the TF'
 570 time series have a best-fitting ARMA model that is pure white noise (i.e., $p = 0$, $q =$
 571 0), and only 3 (<0.1%) have the most complex ARMA model tested (i.e., $p = 4$, $q =$
 572 4) as the best-fitting model.

573 Our goal is to find an ARMA model representative of TF' at a given glacier for
 574 an AOGCM under a specific emission scenario. In other words, we derive a single ARMA
 575 model from the multiple realizations provided by the different ensemble members of an
 576 AOGCM. As explained in Sect. 2.3, we find the across-members optimal ARMA(p^*,q^*)
 577 combination, calibrate it to all ensemble members, and average the noise variance, the
 578 φ_i , and the θ_j coefficients across the different members (see Eq. (28)). To generate a TF'

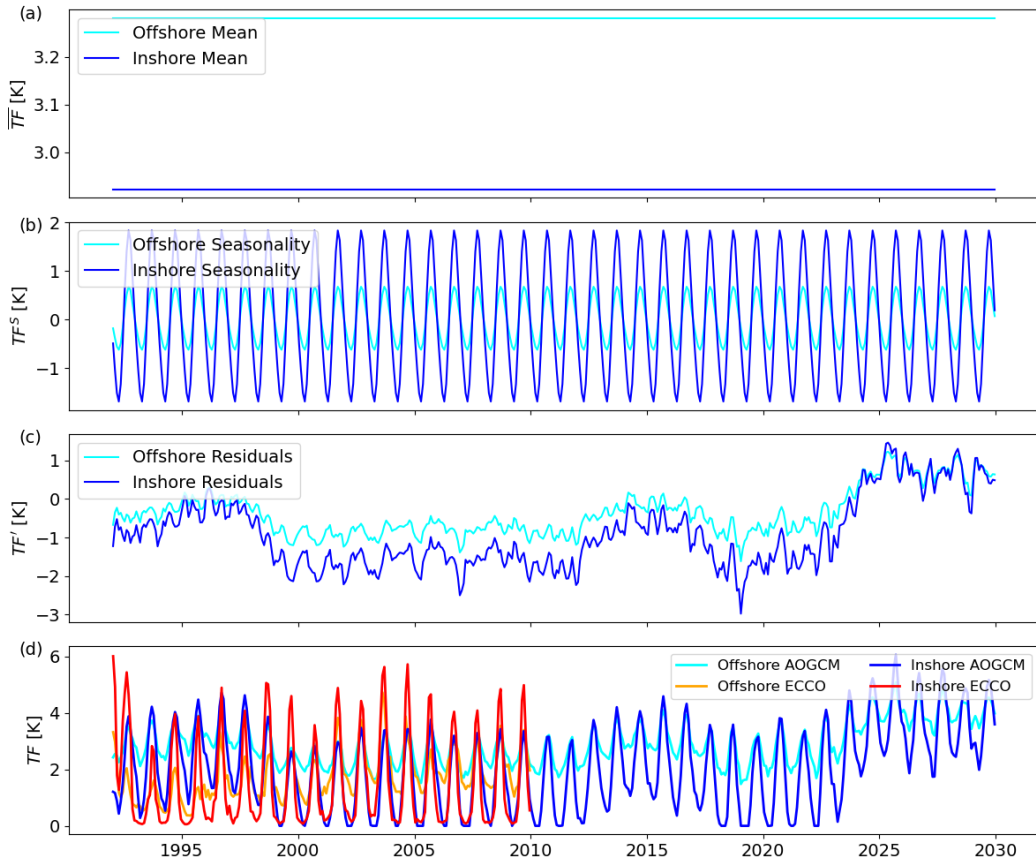


Figure 8. Offshore and extrapolated inshore TF components for r1 member of the IPSL-CM6A AOGCM in emission scenario ssp585, shown at Helheim glacier (see Fig. 1b for location). Time series of (a) offshore and extrapolated inshore mean component (\overline{TF}), (b) offshore and extrapolated inshore seasonality component (TF^S), and (c) offshore and extrapolated inshore residual variability component (TF'). Time series (d) of the total offshore and extrapolated inshore TF . Time series are only shown over the period 1992-2030 for the sake of figure clarity.

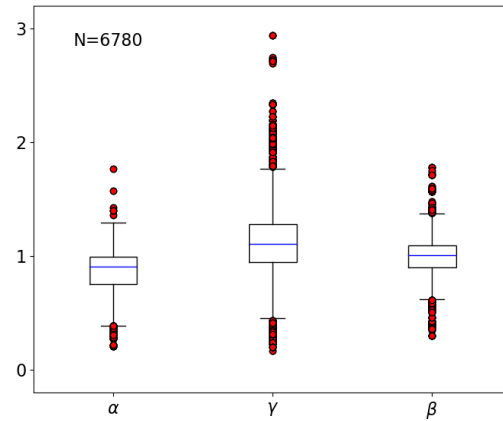


Figure 9. Statistics of the offshore-inshore relations at all glaciers for all the ensemble members of all the AOGCMs in all the emission scenarios considered in this study (total of 6780 offshore-inshore relations). Boxplots of the ratio in \overline{TF} (α , see Eq. (10)), ratio in the sum of absolute monthly effects (γ , see Eq. (13)), and ratio in standard deviation of the residual variability (β , see Eq. (15)).

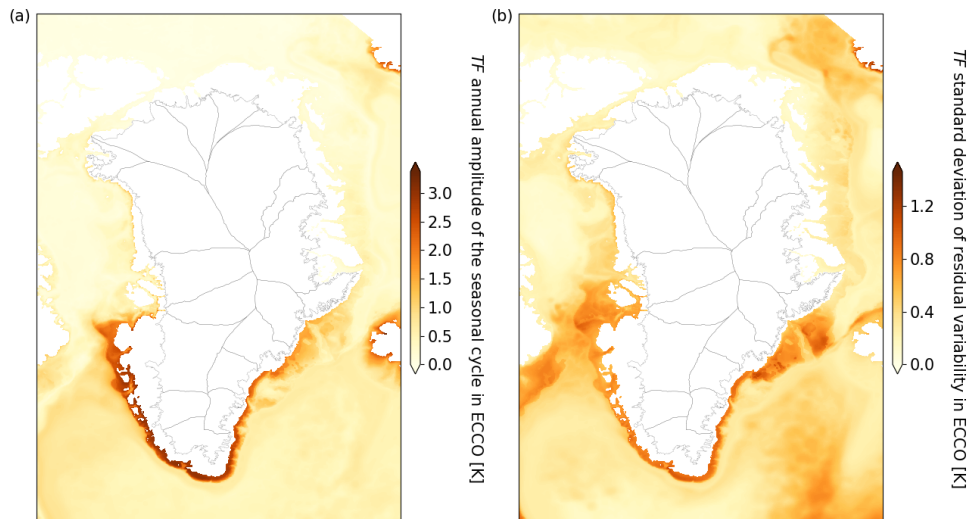


Figure 10. Maps of the high-resolution ($4 \text{ km} \times 4 \text{ km}$) ECCO: (a) amplitude of the seasonal cycle, and (b) standard deviation in the residual variability. The amplitude of the seasonal cycle is half the difference between the maximum and minimum monthly effects (see Eq. (11)).

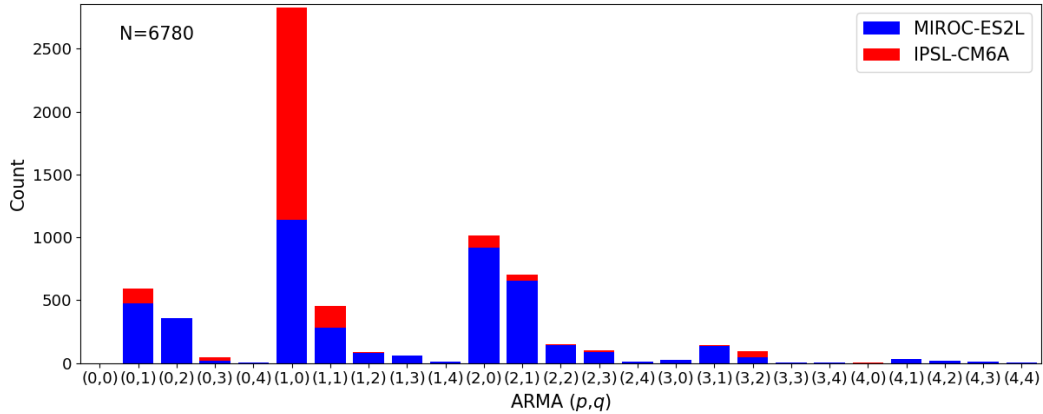


Figure 11. Histograms of best fitting ARMA models for the 6780 QDM-corrected, inshore-extrapolated time series of residual variability in TF . Selection is based on the BIC. The autoregressive order is p , and the moving-average order is q in Eq. (28).

579 time series at a glacier for a given AOGCM-emission scenario combination, we can then
 580 use the ARMA model corresponding to that glacier. Adding back the mean, trend, and
 581 and seasonality component yields a statistically-generated TF time series for the glacier. The
 582 mean-plus-trend (see Eq. (26)) and seasonality components (see Eq. (27)) are taken from
 583 the across-member ensemble mean.

584 The statistically-generated TF' time series are qualitatively similar to the deter-
 585 ministic TF' QDM-corrected inshore-extrapolated time series to which they are calibrated.
 586 This is illustrated in Figure 12a, showing an example of a statistically-generated TF' for
 587 the ARMA model corresponding to IPSL-CM6A in the scenario ssp585 at Helheim glacier.
 588 Subsequently, TF is reconstructed (Fig. 12b) from the ARMA-generated TF' . Both time
 589 series are compared to the corresponding TF and TF' from one of the original IPSL-
 590 CM6A QDM-corrected and inshore-extrapolated ensemble members, which we refer to
 591 as the deterministic time series. These comparisons provide a visual intuition for the abil-
 592 ity of ARMA processes to reproduce the residual variability, and our general fitting pro-
 593 cedure to reproduce the characteristics of TF time series. We also find a good agreement
 594 between the deterministic and statistically-generated TF' in terms of standard devia-
 595 tion and 1-year autocorrelation (Figure 12a). For illustrative purposes, we show statistically-
 596 generated TF time series for a single randomly-selected member of IPSL-CM6A under
 597 ssp585 at six of the largest Greenland outlet glaciers from different regions in Figure 13.
 598 Again, these examples demonstrate that QDM-corrected inshore-extrapolated TF time
 599 series with either deterministic or stochastically-generated residuals are qualitatively sim-
 600 ilar. In contrast, TF of the raw AOGCM from the glaciers' nearest-neighbor locations
 601 show some systematic differences in terms of mean and variability, and can fail to repro-
 602 duce TF values of nearby CTDs (Fig. 13).

603 Quantitatively, we find good agreement in the timescale and amplitude of variabil-
 604 ity between the stochastically-generated TF' and their deterministic counterparts. In
 605 Figure 14a, we compare the 1-year autocorrelation of all the 6780 deterministic TF' time
 606 series of our dataset to a stochastic TF' generated for the corresponding AOGCM, emis-
 607 sion scenario, and glacier. We find that 59% of the variance in the 1-year autocorrela-
 608 tion is explained by the ARMA models, with an RMSE < 0.1 and a bias magnitude < 0.02.
 609 We perform the same comparison for the standard deviation of the time series in Fig-
 610 ure 14b, showing that 89% of the variance is explained, the RMSE is < 0.1 K and the
 611 bias is negligibly small.

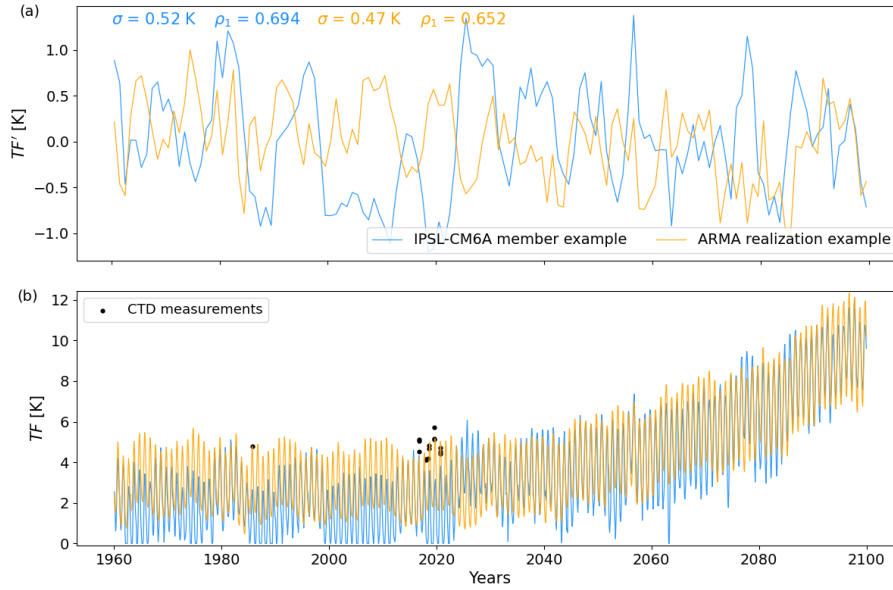


Figure 12. QDM-corrected and inshore-extrapolated time series of (a) TF' and (b) TF using a deterministic ensemble member of IPSL-CM6A under ssp585 at Helheim glacier (blue curves), and a statistically-generated time series using the optimally-calibrated ARMA model (orange curves). The blue TF' curve shows the residual variability as given by the deterministic QDM-corrected and inshore extrapolated AOGCM member, and the orange TF' curve shows the residual variability simulated as an ARMA process. The blue and orange TF curves in panel (b) add the residual variability shown in panel (a) to the mean, trend, and seasonality components. The standard deviation (σ) and 1-year autocorrelation (ρ_1) of the TF' time series are shown in (a). Black dots in (b) show TF measurements from CTD data located at 100 km or less to the glacier front. Time series are only shown over the period 1960-2100 and with a single randomly-selected member for the sake of figure clarity. See Figure 1b for the location of Helheim glacier.

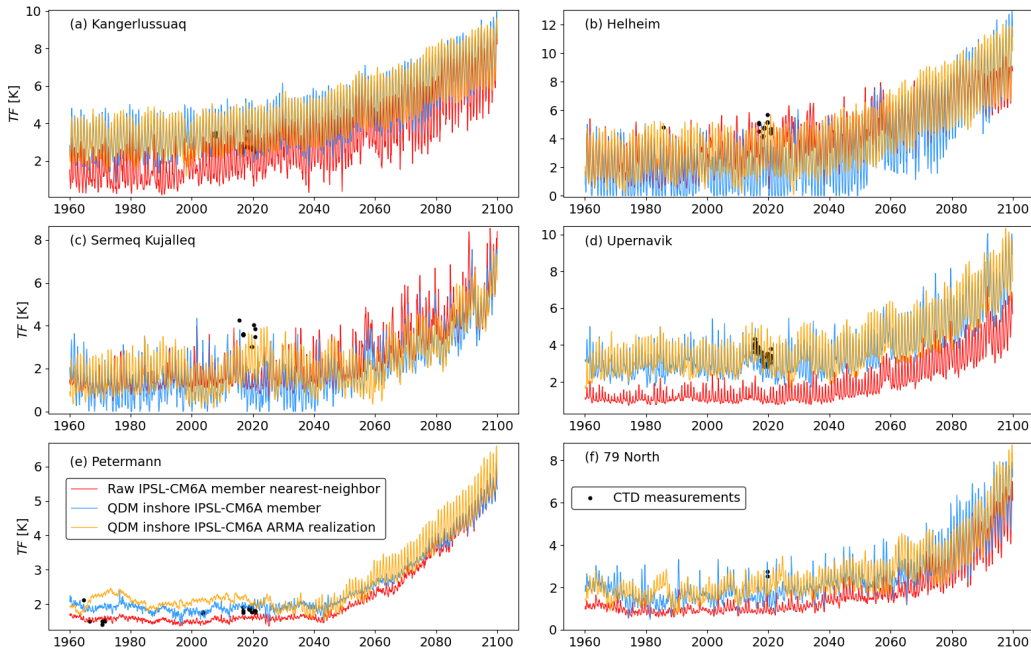


Figure 13. Raw nearest-neighbor AOGCM (red), deterministic QDM-corrected and inshore-extrapolated (light-blue), and ARMA realization of the QDM-corrected and inshore-extrapolated (orange) time series of TF at six large Greenland glaciers in different oceanic sectors. Time series are for the IPSL-CM6A AOGCM under the ssp585 emission scenario. The orange curves use a statistically-generated time series of TF' using the optimally-calibrated ARMA models for each glacier. The blue curves use the residual variability as given by the deterministic QDM-corrected and inshore-extrapolated AOGCM member as TF' . Both the orange and blue curves add their respective TF' to the mean, trend, and seasonality components, resulting in their respective TF time series. Black dots show TF measurements from CTD data located at 100 km or less to the glacier front. Time series are only shown over the period 1960-2100 and with a single randomly-selected member for the sake of figure clarity. See Figure 1b for locations of the glaciers.

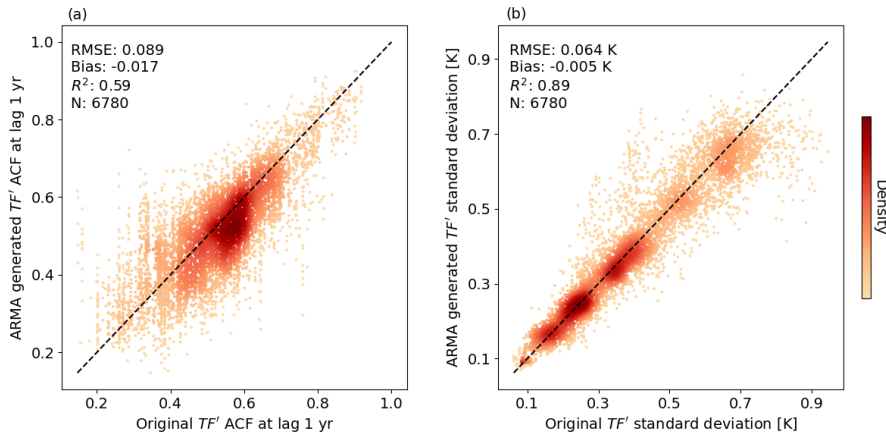


Figure 14. Comparison of (a) autocorrelation function at lag 1-year, and (b) standard deviation. Each pairwise comparison consists of a deterministic TF' time series and a TF' time series generated from the corresponding calibrated ARMA model. RMSE, R^2 , and N denote root mean squared error, coefficient of determination, and total number of pairwise comparisons, respectively.

612 Finally, the correlation matrices (\hat{C} , see Eq. (31)) show that the graphical lasso method
 613 (see Sect. 2.3, Friedman et al., 2008) effectively reduces the empirical correlation struc-
 614 ture and prevents overfitting caused by the small sample size. This is illustrated by compar-
 615 ing the empirical and sparse correlation matrices in Fig. 15 for the case of the IPSL-
 616 CM6A AOGCM under the ssp585 emission scenario. Furthermore, the correlation mat-
 617 rices provide further evidence that our method effectively isolates the residual compo-
 618 nent of TF variability. As shown in the four sparse correlation matrices (Fig. 16), the
 619 correlation structure is similar for a single AOGCM under different emission scenarios,
 620 but differs between AOGCMs. The independence of \hat{C} on the emission scenario can only
 621 be obtained if the non-stationary deterministic changes associated to the emission sce-
 622 nario are removed. This is achieved here by removing polynomials with glacier-specific
 623 parameters in Eqs. (26) and (27), which adequately capture the non-stationary patterns.
 624 In contrast, the correlation patterns differ between AOGCMs, as expected due to their
 625 different internal dynamics. For example, Fig. 16 shows that correlation in IPSL-CM6A
 626 extends over a smaller neighborhood than in MIROC-ES2L.

627 4 Discussion

628 The method developed in this study is complementary to, and extends previous
 629 work for parameterizing ocean thermal forcing in Greenland ice sheet model simulations
 630 (Rignot et al., 2016; Slater et al., 2019, 2020). The QDM correction adjusts the distri-
 631 bution of AOGCM TF with respect to observational datasets, the extrapolation method
 632 corrects for too-coarse model resolution, and stochastic realizations of residual variabil-
 633 ity in TF sample internal climatic variability in model projections. These steps are in-
 634 dependent of each other, and can be performed individually. While the melt parameter-
 635 ization of Xu et al. (2012) and Rignot et al. (2016) assumes that TF is given at the fjord
 636 mouth, the retreat parameterization of Slater et al. (2019) depends on sector-averaged
 637 values. The latter approach could therefore skip the extrapolation step, or alternatively
 638 be re-calibrated while accounting for extrapolation. Furthermore, each step can be ap-
 639 plied with any choice of model and reanalysis products, making the method highly flex-
 640 ible. The accuracy of the TF time series generated depends directly on the quality of

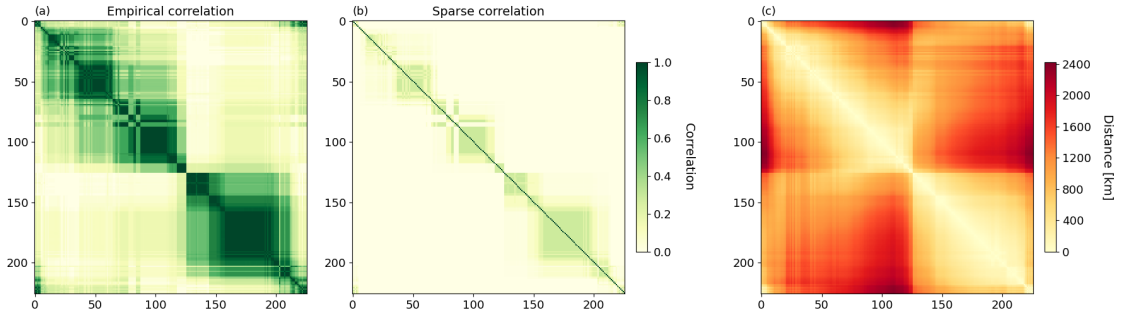


Figure 15. Across-members average of the (a) empirical and (b) sparse correlation matrices for the residual variability between the 226 outlet glacier locations of the IPSL-CM6A AOGCM under the emission scenario ssp585. Numbers on the x- and y-axis denote glacier number, with 0 corresponding to the Northern-most glacier, and glacier numbers increase in the clock-wise direction. Distances between glaciers are shown in (c). The separation around number 125 corresponds to the transition from East to West Greenland. See Fig. 1a for the glacier locations.

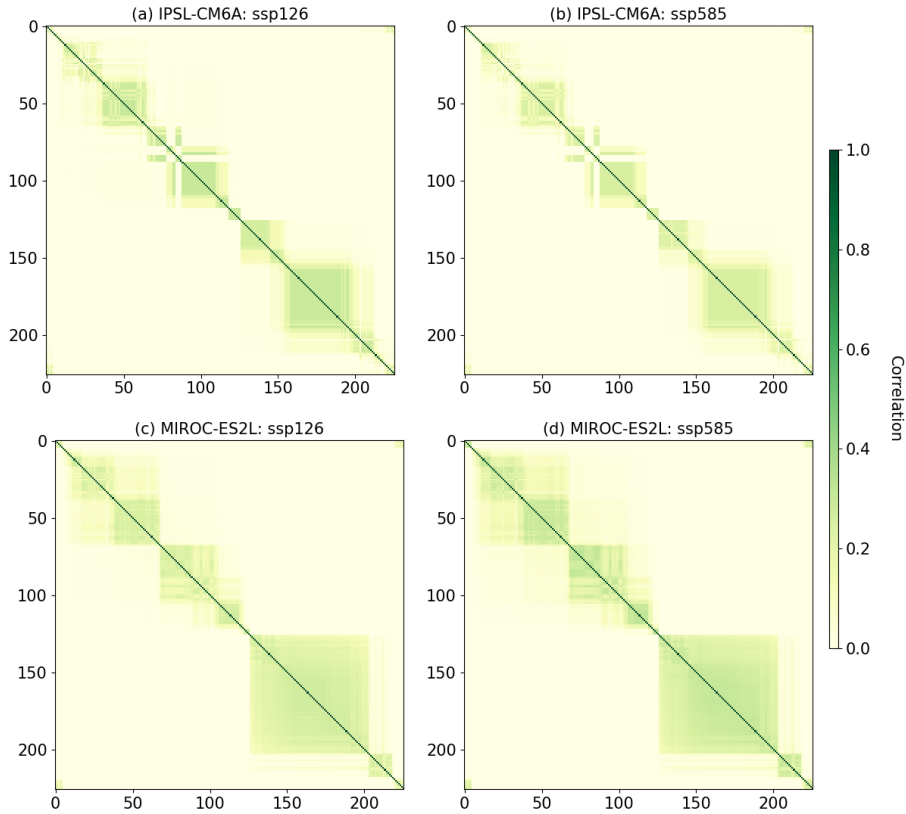


Figure 16. Across-members average of the sparse correlation matrices for the residual variability (\hat{C}) between the 226 outlet glacier locations of the results from (a) IPSL-CM6A under scenario ssp126, (b) IPSL-CM6A under scenario ssp585, (c) MIROC-ES2L under scenario ssp126, and (d) MIROC-ES2L under scenario ssp585. Numbers on the x- and y-axis denote glacier number, with 0 corresponding to the Northern-most glacier, and glacier numbers increase in the clock-wise direction. The separation around number 125 corresponds to the transition from East to West Greenland. See Fig. 15c for distances between glaciers and Fig. 1a for the glacier locations.

641 the products used. Disagreement between different reanalysis products on ocean heat
 642 content can be particularly high around Greenland (Palmer et al., 2017), and one could
 643 explore the sensitivity of the final TF generated to the reanalysis product used. High-
 644 resolution ocean model outputs are scarce, but are likely to increase in coming years such
 645 that the extrapolation method could use multi-model averages of offshore-inshore rela-
 646 tionships. The low computational expense of the ARMA statistical models also facili-
 647 tates the generation of large numbers of TF time series, efficiently sampling the irreducible
 648 climatic uncertainty associated with natural variability. This is important, as there is
 649 an increased awareness of ice sheet sensitivity to variability in ocean conditions (e.g., Hoff-
 650 man et al., 2019; Robel et al., 2019; Christian et al., 2020), and as numerical tools be-
 651 come available to investigate this sensitivity (Verjans et al., 2022).

652 The QDM correction method is well-established in the climate- and hydrology-modeling
 653 communities (e.g., Gudmundsson et al., 2012; Themeßl et al., 2012; Cannon et al., 2015).
 654 It corrects the distributional properties of AOGCM output, and permits the projection
 655 of future changes without invoking a stationarity assumption. Our independent evalu-
 656 ation of the method against CTD data shows that it increases explained variance from
 657 the AOGCM by $\sim 25\%$ and decreases the RMSE by ~ 0.3 K ($\sim 25\%$). However, one
 658 potential limitation is that it linearly adds AOGCM-projected changes in the future pe-
 659 riod (Eq. (5)), regardless of the model biases in the observational period. This assump-
 660 tion therefore does not correct a potential bias in the long-term climate sensitivity of the
 661 AOGCM. This though, is an intrinsic issue of all projections, and argues for the use of
 662 multiple different AOGCMs to force ice sheet models.

663 The extrapolation method (see Sect. 2.2) offers large flexibility in the formulations
 664 of both the regression parameters in the linear relations (Eqs. (9-15)), as well as of the
 665 criteria used in the predictor selection (Eqs. (18-25)). For example, additional refinements
 666 can be applied to the predictor selection by including connectivity between gridpoints
 667 based on passive tracer advection (Oliver & Holbrook, 2014), or by using multiple off-
 668 shore predictors in a multiple regression method. We perform the calibration of the ARMA
 669 models on the residual variability in TF of the AOGCM time series, here spanning 250
 670 years. Alternatively, residuals could be calibrated from pre-industrial control runs of AOGCMs,
 671 which can be >1000 years long. However, this approach faces the limitation that pre-
 672 industrial control AOGCM simulations cannot be QDM-corrected prior to the ARMA
 673 fitting, as reanalysis products are based on data from the industrial era.

674 Our procedure does not capture two-way interactions between the ocean and the
 675 ice sheet. Input of freshwater due to outlet glacier melt and subglacial discharge are im-
 676 portant components of fjord circulation. This could not only modify TF properties in
 677 shallow waters, but also alter the relationship between TF properties on the continen-
 678 tal shelf and glacier frontal melt (Slater et al., 2018; Wagner et al., 2019; Jackson et al.,
 679 2020). Capturing heat transfer through fjords and up to the ice-ocean boundary layer
 680 will require detailed, high-resolution fjord models in the future (e.g., Cowton et al., 2015;
 681 Zhao et al., 2021). The work presented here is relevant to such future model develop-
 682 ments, as it can provide boundary forcing to fjord models by applying our method to
 683 both ocean temperature and salinity, and thus density and stratification, in a similar man-
 684 ner. Nevertheless, in the current context of ocean modeling, our approach remains con-
 685 sistent with the assumption of the Xu et al. (2012) and Rignot et al. (2016) parameter-
 686 ization that the TF variable is prescribed from the fjord mouth. The interplay of atmo-
 687 spheric and oceanic forcing may also be an important factor in governing outlet glacier
 688 frontal melt, because of the dependence of melt rates to both ocean temperatures and
 689 to subglacial discharge, which is sourced from surface melt (Slater & Straneo, 2022). By
 690 exploiting the statistical nature of our method, covariance of TF with surface melt can
 691 be estimated using output from regional climate models and enforced in the TF gener-
 692 ation. Thus, using ocean and atmospheric model output, correlation can capture inter-

693 actions of TF with variables influencing marine-terminating glacier melt, as well as with
694 variables influencing inland ice sheet mass balance.

695 We provide the entire workflow of QDM-correction, inshore extrapolation, and statistical
696 generation of residuals as open-source code (see *Open Research*). These resources
697 allow potential users to compute TF time series as detailed in this study. Furthermore,
698 we provide ensembles of TF time series at the 226 outlet glaciers for the four combina-
699 tions of AOGCMs (IPSL-CM6A and MIROC-ES2L) and CMIP6 emission scenarios (ssp126
700 and ssp585) used in this study as an open-access dataset (see *Data availability statement*).
701 These ensembles of 1000 members each, spanning 1850-2100, can be used by the glaciol-
702 ogy modeling community to force ice sheet model simulations at the scale of the Green-
703 land ice sheet, or sub-regions of the ice sheet.

704 5 Conclusions

705 We propose a statistical method to estimate ocean thermal forcing for the Green-
706 land ice sheet on a range of different timescales. Starting from AOGCM output, and based
707 on output from ocean reanalysis products and high-resolution models, this method bias-
708 corrects, adjusts distributional properties, extrapolates, captures spatial correlation, and
709 samples variability in ocean thermal forcing. The correction of bias and variability am-
710 plitude via a quantile delta mapping approach reproduces the distributional properties
711 of reanalysis products, while preserving the climate sensitivity of the AOGCM in the form
712 of trends and future changes. The extrapolation method derives simple and independent
713 linear relationships between offshore and inshore thermal forcing at different timescales
714 from a high-resolution ocean model. The relationships are subsequently applied to AOGCM
715 output to estimate ocean conditions at fjord mouth locations. Finally, we use autore-
716 gressive moving-average models to represent the residual variability observed in thermal
717 forcing. These statistical models not only reproduce temporal characteristics in mod-
718 eled residual variability, but also capture spatial covariance in ocean thermal forcing.

719 The workflow developed here offers a complementary approach to glacier melt pa-
720 rameterizations that are applied in ice sheet model simulations. Generation of thermal
721 forcing is computationally straightforward owing to the purely statistical nature of each
722 step in the method, and ensembles of time series accompany this study as a data prod-
723 uct. Given the current state of climate and ocean modeling, ice sheet model predictions
724 will likely continue to face a dearth of long-term high-resolution ocean model output avail-
725 ability. This highlights the need to use statistical techniques in order to bridge the gap
726 between existing climate model output and ice sheet model requirements for boundary
727 forcing. Our method is a first step in this direction. It offers the advantages of relative
728 ease of computation, of addressing several limitations of AOGCMs at once, and of be-
729 ing applicable to any combination of AOGCM, reanalysis product, and high-resolution
730 ocean model.

731 6 Open Research

732 All code (python scripts) to reproduce the method described in this study are avail-
733 able as a Zenodo repository (Verjans, 2023):

734 <https://doi.org/10.5281/zenodo.7808874>

735 The repository includes all intermediary and final output files for member r1 of MIROC-
736 ES2L under scenario ssp585 as an example. The repository also includes samples of 1000
737 TF 1850-2100 time series generated following the method presented at the 226 marine
738 glacier fronts for the four combinations of AOGCMs and CMIP6 emission scenarios used
739 in this study. The raw climate model output from the CMIP6 experiments can be down-
740 loaded from:

741 <https://esgf-node.llnl.gov/search/cmip6/>

742 The raw output of the Hadley Centre EN4.2.1 monthly objective analyses can be down-
 743 loaded from:
 744 <https://www.metoffice.gov.uk/hadobs/en4/download-en4-2-1.html>
 745 Output from the high-resolution ECCO Arctic forward run can be downloaded from:
 746 <https://ecco-group.org/>

747 Acknowledgments

748 This work was funded by a grant from the Heising-Simons Foundation. HS was also funded
 749 by the NSF Navigating the New Arctic Program. Computing resources were provided
 750 by the Partnership for an Advanced Computing Environment (PACE) at the Georgia
 751 Institute of Technology, Atlanta. We thank three anonymous reviewers for providing com-
 752 ments that helped to improve the quality of this study. VV thanks Lizz Ultee for guid-
 753 ance about the graphical lasso method, Hong Zhang for helping with ECCO output pro-
 754 cessing, and John Christian for insights about climate variability.

755 References

- 756 Balmaseda, M. A., Alves, O., Arribas, A., Awaji, T., Behringer, D., Ferry, N., ...
 757 Stammer, D. (2009). Ocean initialization for seasonal forecasts. *Oceanography*,
 758 *22*, 154-159.
- 759 Boucher, O., Servonnat, J., Albright, A. L., Aumont, O., Balkanski, Y., Bastrikov,
 760 V., ... Vuichard, N. (2020). Presentation and evaluation of the ipsl-cm6a-lr
 761 climate model. *Journal of Advances in Modeling Earth Systems*, *12*.
- 762 Box, G., & Jenkins, G. M. (1976). *Time series analysis: Forecasting and control*.
 763 Holden-Day.
- 764 Buch, E. (2002). Present oceanographic conditions in greenland waters. *Scientific*
 765 *Report 02-02*.
- 766 Camus, P., Menéndez, M., Méndez, F. J., Izaguirre, C., Espejo, A., Cánovas, V.,
 767 ... Medina, R. (2014). A weather-type statistical downscaling framework for
 768 ocean wave climate. *Journal of Geophysical Research*, *119*, 7389-7405.
- 769 Cannon, A., Sobie, S. R., & Murdock, T. (2015). Bias correction of gcm precipita-
 770 tion by quantile mapping: How well do methods preserve changes in quantiles
 771 and extremes? *Journal of Climate*, *28*, 6938-6959.
- 772 Castruccio, S., & Stein, M. L. (2013). Global space-time models for climate ensem-
 773 bles. *The Annals of Applied Statistics*, *7*, 1593-1611.
- 774 Cheng, L., Foster, G., Hausfather, Z., Trenberth, K. E., & Abraham, J. P. (2022).
 775 Improved quantification of the rate of ocean warming. *Journal of Climate*.
- 776 Christian, J. E., Robel, A. A., Proistosescu, C., Roe, G. H., Koutnik, M. R., &
 777 Christianson, K. (2020). The contrasting response of outlet glaciers to interior
 778 and ocean forcing. *The Cryosphere*.
- 779 Cottier, F. R., Nilsen, F., Skogseth, R., Tverberg, V., Skardhamar, J., & Svendsen,
 780 H. (2010). Arctic fjords: a review of the oceanographic environment and
 781 dominant physical processes..
- 782 Cowton, T. R., Slater, D. A., Sole, A. J., Goldberg, D. N., & Nienow, P. (2015).
 783 Modeling the impact of glacial runoff on fjord circulation and submarine melt
 784 rate using a new subgrid-scale parameterization for glacial plumes. *Journal of*
 785 *Geophysical Research*, *120*, 796-812.
- 786 Cowton, T. R., Sole, A. J., Nienow, P., Slater, D. A., & Christoffersen, P. (2018).
 787 Linear response of east greenland's tidewater glaciers to ocean/atmosphere
 788 warming. *Proceedings of the National Academy of Sciences*, *115*, 7907 - 7912.
- 789 Cui, B., Toth, Z., Zhu, Y., & Hou, D. (2012). Bias correction for global ensemble
 790 forecast. *Weather and Forecasting*, *27*, 396-410.
- 791 Dickey, D. A., & Fuller, W. A. (1981). Likelihood ratio statistics for autoregressive
 792 time series with a unit root. *Econometrica*, *49*(4), 1057-1072. Retrieved 2022-

- 793 10-28, from <http://www.jstor.org/stable/1912517>
- 794 Dickson, R. R., Osborn, T. J., Hurrell, J. W., Meincke, J., Blindheim, J., Ad-
- 795 landsvik, B., ... Maslowski, W. (2000). The arctic ocean response to
- 796 the north atlantic oscillation. *Journal of Climate*, *13*(15), 2671 - 2696.
- 797 Retrieved from [https://journals.ametsoc.org/view/journals/clim/](https://journals.ametsoc.org/view/journals/clim/13/15/1520-0442_2000_013_2671_taortt_2.0.co_2.xml)
- 798 [13/15/1520-0442_2000_013_2671_taortt_2.0.co_2.xml](https://journals.ametsoc.org/view/journals/clim/13/15/1520-0442_2000_013_2671_taortt_2.0.co_2.xml) doi: 10.1175/
- 799 [1520-0442\(2000\)013\(2671:TAORTT\)2.0.CO;2](https://journals.ametsoc.org/view/journals/clim/13/15/1520-0442_2000_013_2671_taortt_2.0.co_2.xml)
- 800 Fagundes, M., Litvin, S. Y., Micheli, F., Leo, G. A. D., Boch, C., Barry, J. P., ...
- 801 Woodson, C. B. (2020). Downscaling global ocean climate models improves
- 802 estimates of exposure regimes in coastal environments. *Scientific Reports*, *10*.
- 803 Felikson, D., Bartholomaeus, T. C., Catania, G. A., Korsgaard, N. J., Kjær, K. H.,
- 804 Morlighem, M., ... Nash, J. D. (2017). Inland thinning on the greenland ice
- 805 sheet controlled by outlet glacier geometry. *Nature Geoscience*, *10*, 366-369.
- 806 Fettweis, X., Hofer, S., Krebs-Kanzow, U., Amory, C., Aoki, T., Berends, C. J., ...
- 807 Zolles, T. (2020). Grsmbmp: intercomparison of the modelled 1980-2012
- 808 surface mass balance over the greenland ice sheet. *The Cryosphere*.
- 809 Friedman, J. H., Hastie, T. J., & Tibshirani, R. (2008). Sparse inverse covariance es-
- 810 timation with the graphical lasso. *Biostatistics*, *9* 3, 432-41.
- 811 Gillard, L. C., Hu, X., Myers, P. G., & Bamber, J. L. (2016). Meltwater path-
- 812 ways from marine terminating glaciers of the greenland ice sheet. *Geo-*
- 813 *physical Research Letters*, *43*(20), 10,873-10,882. Retrieved from [https://](https://agupubs.onlinelibrary.wiley.com/doi/abs/10.1002/2016GL070969)
- 814 agupubs.onlinelibrary.wiley.com/doi/abs/10.1002/2016GL070969 doi:
- 815 <https://doi.org/10.1002/2016GL070969>
- 816 Goelzer, H., Nowicki, S., Payne, A., Larour, E., Seroussi, H., Lipscomb, W. H., ...
- 817 van den Broeke, M. (2020). The future sea-level contribution of the greenland
- 818 ice sheet: a multi-model ensemble study of ismip6. *The Cryosphere*, *14*(9),
- 819 3071-3096. Retrieved from [https://tc.copernicus.org/articles/14/3071/](https://tc.copernicus.org/articles/14/3071/2020/)
- 820 [2020/](https://tc.copernicus.org/articles/14/3071/2020/) doi: 10.5194/tc-14-3071-2020
- 821 Good, S. A., Martin, M. J., & Rayner, N. A. (2013). En4: Quality controlled ocean
- 822 temperature and salinity profiles and monthly objective analyses with uncer-
- 823 tainty estimates. *Journal of Geophysical Research: Oceans*, *118*(12), 6704-
- 824 6716. Retrieved from [https://agupubs.onlinelibrary.wiley.com/doi/abs/](https://agupubs.onlinelibrary.wiley.com/doi/abs/10.1002/2013JC009067)
- 825 [10.1002/2013JC009067](https://agupubs.onlinelibrary.wiley.com/doi/abs/10.1002/2013JC009067) doi: <https://doi.org/10.1002/2013JC009067>
- 826 Gudmundsson, L., Bremnes, J. B., Haugen, J. E., & Engen-Skaugen, T. (2012).
- 827 Technical note: Downscaling rcm precipitation to the station scale using statisti-
- 828 cal transformations – a comparison of methods. *Hydrology and Earth System*
- 829 *Sciences*, *16*, 3383-3390.
- 830 Hajima, T., Watanabe, M., Yamamoto, A., Tatebe, H., Noguchi, M. A., Abe,
- 831 M., ... Kawamiya, M. (2020). Development of the miroc-es2l earth
- 832 system model and the evaluation of biogeochemical processes and feed-
- 833 backs. *Geoscientific Model Development*, *13*(5), 2197-2244. Retrieved
- 834 from <https://gmd.copernicus.org/articles/13/2197/2020/> doi:
- 835 [10.5194/gmd-13-2197-2020](https://gmd.copernicus.org/articles/13/2197/2020/)
- 836 Hasselmann, K. (1976). Stochastic climate models part i. theory. *Tellus A*, *28*, 473-
- 837 485.
- 838 Hausfather, Z., Cowtan, K. D., Clarke, D. C., Jacobs, P., Richardson, M. I., &
- 839 Rohde, R. A. (2017). Assessing recent warming using instrumentally homoge-
- 840 neous sea surface temperature records. *Science Advances*, *3*.
- 841 Hoffman, M. J., Asay-Davis, X. S., Price, S. F. D., Fyke, J. G., & Perego, M. (2019).
- 842 Effect of subshelf melt variability on sea level rise contribution from thwaites
- 843 glacier, antarctica. *Journal of Geophysical Research: Earth Surface*, *124*, 2798
- 844 - 2822.
- 845 Holland, D. M., Thomas, R. H., de Young, B., Ribergaard, M. H., & Lyberth, B.
- 846 (2008). Acceleration of jakobshavn isbræ triggered by warm subsurface ocean
- 847 waters. *Nature Geoscience*, *1*, 659-664.

- 848 Hu, W., & Castruccio, S. (2021). Approximating the internal variability of bias-
 849 corrected global temperature projections with spatial stochastic generators.
 850 *Journal of Climate*.
- 851 IMBIE. (2020). Mass balance of the greenland ice sheet from 1992 to 2018. *Nature*,
 852 *579*, 233-239.
- 853 Jackson, R. H., Lentz, S. J., & Straneo, F. (2018). The dynamics of shelf forcing in
 854 greenlandic fjords. *Journal of Physical Oceanography*.
- 855 Jackson, R. H., Nash, J. D., Kienholz, C., Sutherland, D. A., Amundson, J. M., Mo-
 856 tyka, R. J., ... Pettit, E. C. (2020). Meltwater intrusions reveal mechanisms
 857 for rapid submarine melt at a tidewater glacier. *Geophysical Research Letters*,
 858 *47*.
- 859 Jackson, R. H., Straneo, F., & Sutherland, D. A. (2014). Externally forced fluctu-
 860 ations in ocean temperature at greenland glaciers in non-summer months. *Nature*
 861 *Geoscience*, *7*, 503-508.
- 862 Jakobsson, M., Macnab, R. F., Mayer, L. A., Anderson, R. M., Edwards, M. H.,
 863 Hatzky, J., ... Johnson, P. (2008). An improved bathymetric portrayal of the
 864 arctic ocean: Implications for ocean modeling and geological, geophysical and
 865 oceanographic analyses. *Geophysical Research Letters*, *35*.
- 866 Kay, J. E., Deser, C., Phillips, A. S., Mai, A., Hannay, C., Strand, G., ... Verten-
 867 stein, M. (2015). The community earth system model (cesm) large ensemble
 868 project: a community resource for studying climate change in the presence of
 869 internal climate variability. *Bulletin of the American Meteorological Society*,
 870 *96*, 1333-1349.
- 871 Maher, N., Milinski, S., Suarez-Gutierrez, L., Botzet, M., Dobrynin, M., Dobrynin,
 872 M., ... Marotzke, J. (2019). The max planck institute grand ensemble: En-
 873 abling the exploration of climate system variability. *Journal of Advances in*
 874 *Modeling Earth Systems*, *11*, 2050 - 2069.
- 875 Marks, K. M., & Smith, W. H. F. (2006). An evaluation of publicly available global
 876 bathymetry grids. *Marine Geophysical Researches*, *27*, 19-34.
- 877 Morlighem, M., Williams, C. N., Rignot, E., An, L., Arndt, J. E., Bamber, J. L., ...
 878 Zinglensen, K. B. (2017). Bedmachine v3: Complete bed topography and ocean
 879 bathymetry mapping of greenland from multibeam echo sounding combined
 880 with mass conservation. *Geophysical Research Letters*, *44*, 11051 - 11061.
- 881 Mouginot, J., Rignot, E., Björk, A. A., van den Broeke, M. R., Millan, R.,
 882 Morlighem, M., ... Wood, M. (2019). Forty-six years of greenland ice sheet
 883 mass balance from 1972 to 2018. *Proceedings of the National Academy of*
 884 *Sciences of the United States of America*, *116*, 9239 - 9244.
- 885 Mudelsee, M. (2010). Climate time series analysis: Classical statistical and boot-
 886 strap methods. *Climate Time Series Analysis*.
- 887 Nguyen, A. T., Kwok, R., & Menemenlis, D. (2012). Source and pathway of the
 888 western arctic upper halocline in a data-constrained coupled ocean and sea ice
 889 model. *Journal of Physical Oceanography*, *42*, 802-823.
- 890 Nick, F. M., Vieli, A., Howat, I. M., & Joughin, I. R. (2009). Large-scale changes
 891 in greenland outlet glacier dynamics triggered at the terminus. *Nature Geo-*
 892 *science*, *2*, 110-114.
- 893 Noël, B. P. Y., van de Berg, W. J., Machguth, H., Lhermitte, S., Howat, I. M., Fet-
 894 tweis, X., & van den Broeke, M. (2016). A daily, 1 km resolution data set
 895 of downscaled greenland ice sheet surface mass balance (1958-2015). *The*
 896 *Cryosphere*, *10*, 2361-2377.
- 897 Oliver, E. C. J., & Holbrook, N. J. (2014). A statistical method for improving conti-
 898 nental shelf and nearshore marine climate predictions. *Journal of Atmospheric*
 899 *and Oceanic Technology*, *31*, 216-232.
- 900 Palmer, M. D., Roberts, C. D., Balmaseda, M. A., Chang, Y.-S., Chepurin, G. A.,
 901 Ferry, N., ... Xue, Y. (2017). Ocean heat content variability and change in an
 902 ensemble of ocean reanalyses. *Climate Dynamics*, *49*, 909-930.

- 903 Porter, D. F., Tinto, K. J., Boghosian, A. L., Csathó, B. M., Bell, R. E., & Cochran,
904 J. R. (2018). Identifying spatial variability in greenland’s outlet glacier re-
905 sponse to ocean heat. *Frontiers in Earth Science*.
- 906 Rignot, E., Fenty, I. G., Menemenlis, D., & Xu, Y. (2012). Spreading of warm ocean
907 waters around greenland as a possible cause for glacier acceleration. *Annals of*
908 *Glaciology*, *53*, 257 - 266.
- 909 Rignot, E., Xu, Y., Menemenlis, D., Mouginot, J., Scheuchl, B., Li, X., . . . de
910 Fleurian, B. (2016). Modeling of ocean-induced ice melt rates of five west
911 greenland glaciers over the past two decades. *Geophysical Research Letters*, *43*,
912 6374 - 6382.
- 913 Robel, A. A., Seroussi, H., & Roe, G. H. (2019). Marine ice sheet instability ampli-
914 fies and skews uncertainty in projections of future sea-level rise. *Proceedings of*
915 *the National Academy of Sciences of the United States of America*, *116*, 14887
916 - 14892.
- 917 Schwarz, G. (1978). Estimating the dimension of a model. *The Annals of Statistics*,
918 *6*(2), 461–464. Retrieved 2022-10-28, from [http://www.jstor.org/stable/](http://www.jstor.org/stable/2958889)
919 [2958889](http://www.jstor.org/stable/2958889)
- 920 Shapiro, S. S., & Wilk, M. B. (1965). An analysis of variance test for normality
921 (complete samples). *Biometrika*, *52*, 591-611.
- 922 Slater, D. A., Felikson, D., Straneo, F., Goelzer, H., Little, C. M., Morlighem, M.,
923 . . . Nowicki, S. M. J. (2020). Twenty-first century ocean forcing of the green-
924 land ice sheet for modelling of sea level contribution. *The Cryosphere*.
- 925 Slater, D. A., & Straneo, F. (2022). Submarine melting of glaciers in greenland ampli-
926 fied by atmospheric warming. *Nature Geoscience*, *15*, 794 - 799.
- 927 Slater, D. A., Straneo, F., Das, S. B., Richards, C. G., Wagner, T., & Nienow, P.
928 (2018). Localized plumes drive front-wide ocean melting of a greenlandic
929 tidewater glacier. *Geophysical Research Letters*, *45*, 12,350 - 12,358.
- 930 Slater, D. A., Straneo, F., Felikson, D., Little, C. M., Goelzer, H., Fettweis, X., &
931 Holte, J. (2019). Estimating greenland tidewater glacier retreat driven by
932 submarine melting. *The Cryosphere*.
- 933 Storch, H. v., & Zwiers, F. W. (1999). *Statistical analysis in climate research*. Cam-
934 bridge University Press. doi: 10.1017/CBO9780511612336
- 935 Straneo, F., & Cenedese, C. (2015). The dynamics of greenland’s glacial fjords and
936 their role in climate. *Annual review of marine science*, *7*, 89-112.
- 937 Straneo, F., & Heimbach, P. (2013). North atlantic warming and the retreat of
938 greenland’s outlet glaciers. *Nature*, *504*, 36-43.
- 939 Straneo, F., Slater, D. A., Bouchard, C., Cape, M. R., Carey, M., Ciannelli, L., . . .
940 Vernet, M. (2022). An interdisciplinary perspective on greenland’s changing
941 coastal margins. *Oceanography*.
- 942 Straneo, F., Sutherland, D. A., Holland, D. M., Gladish, C. V., Hamilton, G., John-
943 son, H. L., . . . Koppes, M. N. (2012). Characteristics of ocean waters reaching
944 greenland’s glaciers. *Annals of Glaciology*, *53*, 202 - 210.
- 945 Strass, V. H., Fahrbach, E., Schauer, U., & Sellmann, L. (1993). Formation of den-
946 mark strait overflow water by mixing in the east greenland current. *Journal of*
947 *Geophysical Research*, *98*, 6907-6919.
- 948 Sutherland, D. A., Roth, G., Hamilton, G., Mernild, S. H., Stearns, L. A., & Stra-
949 neo, F. (2014). Quantifying flow regimes in a greenland glacial fjord using
950 iceberg drifters. *Geophysical Research Letters*, *41*, 8411 - 8420.
- 951 Sutherland, D. A., Straneo, F., Stenson, G. B., Davidson, F. J. M., Hammill, M. O.,
952 & Rosing-Asvid, A. (2013). Atlantic water variability on the se greenland
953 continental shelf and its relationship to sst and bathymetry. *Journal of Geo-*
954 *physical Research*, *118*, 847-855.
- 955 Themeßl, M. J., Gobiet, A., & Heinrich, G. (2012). Empirical-statistical downscaling
956 and error correction of regional climate models and its impact on the climate
957 change signal. *Climatic Change*, *112*, 449-468.

- 958 Tsai, C.-Y., Forest, C. E., & Pollard, D. D. (2017). Assessing the contribution of
 959 internal climate variability to anthropogenic changes in ice sheet volume. *Geo-*
 960 *physical Research Letters*, *44*, 6261-6268.
- 961 Verjans, V. (2023). Code for Bias correction and statistical modeling of variable
 962 oceanic forcing of greenland outlet glaciers: April 07, 2023 Release (Version
 963 1.0) [Software]. Zenodo.
 964 doi: <https://doi.org/10.5281/zenodo.7808874>
- 965 Verjans, V., Robel, A. A., Seroussi, H., Ultee, L., & Thompson, A. F. (2022). The
 966 stochastic ice-sheet and sea-level system model v1.0 (stissm v1.0). *Geoscientific*
 967 *Model Development*, *15*(22), 8269–8293. doi: 10.5194/gmd-15-8269-2022
- 968 Wagner, T. J. W., Straneo, F., Richards, C. G., Slater, D. A., Stevens, L. A., Das,
 969 S. B., & Singh, H. (2019). Large spatial variations in the flux balance along
 970 the front of a greenland tidewater glacier. *The Cryosphere*.
- 971 Walsh, K. M., Howat, I. M., Ahn, Y., & Enderlin, E. M. (2012). Changes in
 972 the marine-terminating glaciers of central east greenland, 2000–2010. *The*
 973 *Cryosphere*, *6*, 211-220.
- 974 Wilks, D. S. (2011). *Statistical methods in atmospheric sciences*. Academic Press.
- 975 Wood, M., Rignot, E., Fenty, I. G., An, L., Bjørk, A. A., van den Broeke, M. R., . . .
 976 Zhang, H. (2021). Ocean forcing drives glacier retreat in greenland. *Science*
 977 *Advances*, *7*.
- 978 Xu, Y., Rignot, E., Menemenlis, D., & Koppes, M. N. (2012). Numerical exper-
 979 iments on subaqueous melting of greenland tidewater glaciers in response to
 980 ocean warming and enhanced subglacial discharge. *Annals of Glaciology*, *53*,
 981 229 - 234.
- 982 Zhao, K., Stewart, A. L., & McWilliams, J. C. (2021). Linking overturning, recircu-
 983 lation, and melt in glacial fjords. *Geophysical Research Letters*, *49*.